Increased spatiotemporal resolution reveals highly dynamic dense tubular matrices in the peripheral ER

Authors: Jonathon Nixon-Abell[1,2]†, Christopher J. Obara[3,4]†, Aubrey V. Weigel[3,4]†, Dong Li[4,5], Wesley R. Legant[4], C. Shan Xu[4], H. Amalia Pasolli[4], Kirsten Harvey[2], Harald F. Hess[4], Eric Betzig[4], Craig Blackstone[1]‡*, Jennifer Lippincott-Schwartz[3,4]‡*

Affiliations:

[1]Cell Biology Section, Neurogenetics Branch, NINDS, NIH
[2]Department of Pharmacology, UCL School of Pharmacy, UCL
[3]Cell Biology and Metabolism Program, Eunice Kennedy Shriver NICHD, NIH
[4]Janelia Research Campus, HHMI
[5]National Laboratory of Biomacromolecules, Institute of Biophysics, Chinese Academy of Sciences
†Equal Contribution.
‡Equal Contribution.

*Correspondence to:

Craig Blackstone
NIH Building 35, Room 2A-201
9000 Rockville Pike,
Bethesda, MD 20892
blackstc@ninds.nih.gov

Jennifer Lippincott-Schwartz
HHMI Janelia Research Campus
19700 Helix Drive
Ashburn, VA 20147
lippincottschwartzj@janelia.hhmi.org

Abstract (125 words):

The endoplasmic reticulum (ER) is an expansive, membrane-enclosed organelle, playing crucial roles in numerous cellular functions. We employ emerging superresolution imaging technologies to clarify the morphology and dynamics of the peripheral ER, which contacts and modulates most other intracellular organelles. Peripheral components of the ER have classically been described as comprising both tubules and flat sheets. We show this system consists almost exclusively of tubules at varying densities, including newly characterized structures we term ER matrices. These structures have been misidentified as sheets with conventional optical imaging technologies due to the dense clustering of tubular junctions and a previously uncharacterized rapid form of ER motion. Furthermore, the existence of matrices

explains previous confounding evidence where proliferation of ER "sheets" occurs following overexpression of tubular junction-forming proteins.

One Sentence Summary: Superresolution imaging reveals that structures in the ER classically identified as peripheral sheets are, in fact, dense matrices of highly-dynamic tubules and three-way junctions.

Main Text:

The ER is a continuous, membranous network extending from the nuclear envelope to the outer periphery of cells, playing vital roles in processes such as protein synthesis and folding, mitochondrial division, calcium storage and signaling, and lipid synthesis and transfer. In the cell periphery, the ER is thought to exist as an elaborate membrane system that makes contact with nearly every other cellular organelle. Prevailing models of its structure propose a complex arrangement of interconnected tubules and sheets, each of which is maintained by distinct mechanisms (*1*, *2*). Numerous proteins are involved in maintaining this complex structural organization. Membrane curvature-stabilizing proteins including members of the reticulon (RTN) and REEP families contain hydrophobic hairpin domains that are considered responsible for promoting curvature in ER tubules via scaffolding and hydrophobic wedging. Members of the atlastin (ATL) family of dynamin-related GTPases are thought to mediate the formation of three-way junctions between tubules, giving rise to the characteristic polygonal tubular network (*3*). Meanwhile, an alternative complement of proteins is proposed to regulate the structure of ER sheets, with p180, kinectin and CLIMP63 all thought to play a role in shaping, helicoidal stacking and luminal spacing (*3*). Crucially, mutations in many of these ER shaping proteins are connected to a variety of human disease conditions, most notably the hereditary spastic paraplegias (HSPs) (*4*). Thus, characterizing ER morphology is critical in understanding the basic biology of cells in both health and disease.

Determining ER structure presents a significant challenge given limitations in our current ability to visualize the intricate nature of its morphology. The peripheral ER is particularly susceptible to this constraint given its well-documented dynamic rearrangements and fine ultrastructure (*5*, *6*). Attempts to derive functional information based on changes to ER structure are thus significantly hampered. The recent development of various superresolution (SR) imaging approaches, however, presents the opportunity to examine ER structure and dynamism with significantly improved spatiotemporal resolution. Here, we employ five different SR modalities, each having complementary strengths and weaknesses in the spatial and temporal domains, to examine ER structure and dynamics. A high-speed variation of Structured Illumination Microscopy (SIM) allowed ER dynamics to be visualized at unprecedented speeds and resolution. Three-dimensional SIM and Airyscan imaging allowed the fine distributions of different ER-shaping proteins to be compared. Finally, Lattice Light Sheet-Point Accumulation for Imaging in Nanoscale Topography (LLS-PAINT) and Focused Ion Beam-Scanning Electron Microscopy (FIB-SEM) permitted three-dimensional characterization of different ER structures. Thoroughly probing the ER in this manner

provides unprecedented information about the morphology and dynamics of this organelle, including the characterization of a previously underappreciated structure within the peripheral ER.

ER tubules and junctions undergo rapid motion in living cells

ER tubules are known to undergo rapid structural rearrangements, occurring over seconds or minutes, yet examination of these processes has typically been confined to the extension/retraction of tubules and the formation of tubular three-way junctions (*5*, *6*). To obtain a more comprehensive picture of tubular motion, we employed high-speed SIM with grazing incidence illumination (GI-SIM - see Supplementary Methods) (*7*). This live SR imaging modality (~100 nm resolution) uses light beams counter-propagating just above the sample substrate to image cellular features near the basal plasma membrane at frequencies up to 40 Hz. This translates to a 4- to 10-fold higher acquisition speed than we find practically achievable for imaging the ER using spinning disk confocal microscopy, and about a two-fold improvement in resolution.

With GI-SIM, we imaged COS-7 cells expressing an ER membrane marker (mEmerald-Sec61β, henceforth Sec61β) to track ER tubules. Increased spatiotemporal resolution revealed a novel form of ER motion consisting of remarkably rapid tubular fluctuations (Fig. 1, movie S1). Using a modified skeletonization algorithm (*8*) to track the movement of ER tubules (Fig. 1B), we identified oscillations with a mean peak-to-peak amplitude of 70 ± 50 nm, occurring an average of 4 ± 1 times per second (means ± s.d.; Fig. 1, C and D, n = 1755 tubules from 8 cells). Traditional imaging modalities have the ability to localize precisely this tubular motion only if the tubules and junctions are sufficiently sparse. Also, a significant proportion of this motion often occurs on too short a timescale to be effectively tracked using spinning disk confocal microscopy at imaging speeds commonly reported in the literature (*6*, *9*). This suggests that in dense regions tubular ER motion and morphology are likely to be obscured when using traditional imaging modalities. These rapid fluctuations we observed in COS-7 cells were also found in an unrelated cell type (U-2 OS) as well as in COS-7 cells expressing a luminal ER marker (mEmerald-ER3, henceforth ER3; see Materials and Methods) instead of Sec61β (Fig. 1, C-E; tables S1 and S2).

In addition to the tubules themselves, three-way junctions also exhibit appreciable motion over very short timescales (Figs. 1, F and G; movie S1). Three-way junctions were identified from the skeletonization of fluorescent ER images. Skeletonized pixels with exactly two neighbors were considered to be part of a branch (Fig. 1F, white), and pixels with more than two neighbors were considered junctions (Fig. 1F, overlaid with cyan dots). Three-way junctions were then treated as single particles and tracked (Fig. 1F, green). The time-averaged mean square displacement (MSD) of three-way junctions can be described as $MSD \sim t^{\alpha}$ where α can be used to describe a particle's motion as Brownian ($\alpha = 1$), subdiffusive ($\alpha < 1$), or superdiffusive ($\alpha > 1$) (*10*). Junction dynamics exhibit a broad distribution of α (Fig. 1G; table S1). Again, these results were consistent among cells expressing membrane or luminal markers as well as in other cell types such as U-2 OS (Fig. 1G; tables S1 and S2).

Such rapid dynamics can often represent thermally-derived motion in systems, but in this context thermal energy alone does not appear to be responsible for driving ER dynamics. Indeed, the above characterized motion of both tubules and three-way

junctions was substantially altered by a variety of biological perturbations. Diverse treatments affecting access to cellular energy sources (DOG + NaN_3, AlF), cytoskeletal dynamics (blebbistatin), or protein translation (puromycin, cycloheximide) each reduced the amplitude and increased the frequency of oscillations to levels consistent with thermally-derived Brownian motion (*11*) (Fig. 1; C-E). Additionally, the motion of three-way junctions was dampened (Fig. 1G). While the broad susceptibility of rapid ER dynamics to pharmacological perturbation does not elucidate the direct source of the motion, it suggests a broader role for cellular dynamics in driving ER motion, as it is affected by a range of disparate processes. Of note, treatment with the microtubule depolymerizing agent nocodazole increased the frequency of motion without any noticeable effect on amplitude (Fig. 1E; table S2), so it appears that at least in some situations the amplitude and frequency of tubule oscillations can be uncoupled.

Peripheral "sheets" appear highly dynamic and are riddled with spaces

GI-SIM also permitted rapid imaging of the morphology and dynamics of structures that appeared to be flat peripheral sheets by diffraction-limited epifluorescence, leading to several highly unexpected observations. Importantly, at the improved spatiotemporal resolution afforded by GI-SIM, most peripheral "sheets" do not appear continuous, but rather are riddled throughout with spaces devoid of Sec61β fluorescence (Fig. 2, A and B). These spaces are highly dynamic and densely distributed across the structure (Fig. 2B kymographs). To analyze these dynamics, a fluorescence inversion and image preparation protocol was employed (see Materials and Methods) (*12*), transforming the dark areas into particle-like entities that are trackable using single-particle tracking (SPT) algorithms (*13*) (Fig. 2C, movie S2). The spaces were tracked and, from the trajectories, their lifetimes were extracted. For distances between tubules (spaces) larger than our ~100 nm limit of resolution, the average lifespan (250 ± 250 ms, n = 4,292 tracks from 4 cells) and detectable separation between tubules (260 ± 350 nm, n = 1,273 spaces from 4 cells) was quantified (Fig. 2D; tables S3 and S4). There was no significant difference in the lifespan or apparent size of voids in intensity in either U-2 OS or COS-7 cells expressing Sec61β (table S4). Measurable gaps between tubules did, however, appear significantly smaller in cells expressing Sec61β than in cells expressing ER3, presumably due to the relocation of the fluorescence tag from the lumen to the cytoplasmic surface of the ER membrane (Fig. 2D, tables S3 and S4, discussed further in Supplementary Text). This apparent dilatation of the structure would be predicted to lead to an appearance of constriction in remaining non-fluorescent spaces. Certainly, the size and lifetime of the spaces observed with GI-SIM within these peripheral structures renders a significant proportion of them undetectable by more traditional imaging modalities.

To accompany the SPT of these transient spaces, we utilized an analysis that does not require a best-fit process, termed Temporal Intensity Derivative (detailed in Materials and Methods, fig. S1). This technique maps locations in the structure where substantial changes in fluorescence intensity occur over defined time windows. We found that even across a very short (250 ms) timeframe, we were able to detect substantial motion in ER tubules, consistent with the tubular oscillations described in Fig. 1. Intriguingly, nearly the entire area of structures that appeared as peripheral "sheets" by conventional imaging also underwent fluctuations in fluorescence intensity similar to that of isolated tubules,

suggesting significant structural rearrangements within these structures over this time frame (Fig. 2, E and F). This phenomenon was consistently observed in COS-7 cells expressing either Sec61β or ER3, and in U-2 OS cells expressing Sec61β. Collectively, the rapid rearrangement of spaces and the magnitude of fluorescence changes across very short time scales within peripheral sheet-like structures imply that these regions are not likely to be continuous in nature.

Rapid assembly and disassembly of sheet-like structures into isolated tubules

In further support of this, longer time-lapse imaging using GI-SIM reveals rapid assembly and disassembly of sheet-like structures from clearly isolated tubules (movie S3). This process occurs over relatively short time frames. As such, it seems unlikely that energetically costly fusion or fission of the ER membrane would be required. Instead, our data suggest a possible mechanism whereby tubules could coalesce until the spaces between them become too small to observe, leading to the discontinuities described above. Consequently, dense networks could expand outwards to isolated tubules by the reverse mechanism, without requiring membrane fusion or fission. This could be achieved by well-characterized motion through molecular motors or by the sliding of three-way junctions along tubules (*3*).

SR imaging reveals the existence of dense tubular matrices in the peripheral ER

In order to gain a more comprehensive understanding of structures classically defined as peripheral sheets, we performed parallel experiments to reconstruct the protein and lipid distribution across the entire ER using SR imaging. COS-7 cells expressing Sec61β as an ER marker (thought to be expressed uniformly across the ER) were fixed and imaged by three-dimensional, wide-field SIM (3D-SIM), providing a representative map of ER transmembrane protein distribution throughout the cell (Fig. 3A). Remarkably, many structures that appeared to be intact sheets by diffraction-limited, wide-field imaging instead comprised a dense, cross-linked network of tubules enriched in three-way junctions (Fig. 3A). Notably, these structures are relatively flat compared to their height, but show some substantial variation in local topology when the three-dimensional structure is shown (Fig. 3A, color coding).

To verify that the ER membrane itself shared this structure, we turned to an even higher resolution imaging technique that directly probes the locations of the membranes themselves. LLS-PAINT microscopy utilizes single molecule localization of individual fluorescent lipid molecules as they stabilize on cellular membranes (*14*). COS-7 cells expressing Sec61β were fixed and the structure of the internal membranes was ascertained at the single molecule level using LLS-PAINT microscopy (movie S4). In addition, for each cell a single diffraction-limited 3D LLS image (*15*) was taken of the Sec61β signal to allow ER membranes to be distinguished from those of other organelles (Fig. 3B, movie S4). The resulting data set confirms that many ER structures that appear as continuous sheets with diffraction-limited imaging, when viewed using LLS-PAINT, are dense tubular matrices (Fig. 3B, insets). Of note, many ER matrices had substantial topological variation across their structures, again supporting the notion they are not strictly two-dimensional (Fig. 3Biii and fig. S2). Thus, with improved spatial resolution in three dimensions, both protein and lipid components of the peripheral ER appear to comprise dense matrices of highly-convoluted tubules.

Limitations in spatiotemporal resolution obscure dense tubular matrices

Given our observations that ER tubules undergo very rapid motion (Fig. 1), that many spaces in structures previously described as sheets are near or beneath the diffraction limit (Fig. 2), and that SR imaging of both ER membrane protein and lipid reveals most of these structures to be dense tubular networks (Fig. 3), we hypothesized that limitations in spatiotemporal resolution might obscure dense tubular matrices and lead to their frequent misinterpretation as sheets. To test this directly, we compared images of peripheral ER matrices collected by either diffraction-limited GI or GI-SIM using two different simulated exposure times (see Materials and Methods for details) (Fig. 4A). We found that the loss of either spatial or temporal resolution was, in fact, sufficient to obscure the majority of gaps between tubules within the matrix.

In the case of live-cell imaging, tubular motion can occur faster than the acquisition time of a single frame, creating a blurring artifact and thus increasing the apparent diameter of tubules as the temporal resolution decreases (Fig. 4B; tables S5 and S6). Likewise, the resolvable separation between tubules in a matrix is affected not only by the true distance across the space between tubules, but also by temporal blurring due to oscillations of the surrounding tubules and motion of their three-way junctions. We therefore expected gaps in tight tubular matrices to appear smaller in active, living cells than in fixed ones. Indeed, the average apparent distance between tubules in fixed 3D-SIM (220 nm) was ~ 1.5-fold greater than that observed using live GI-SIM (150 nm). Consequently, we predicted that decreasing temporal resolution would preferentially blur smaller spaces, as tubular oscillations and junction movement would mask them more readily. To quantify this, we summed GI-SIM images of tubular matrices over an increasing number of 25 ms frames to simulate longer exposure times. As predicted, longer simulated exposure times resulted in blurring of matrices until they ultimately resembled continuous sheets (Fig. 4D). On the other hand, improving temporal resolution decreased the minimum distance required between tubules before a space became detectable (Fig. 4E; tables S5 and S6), increasing the density of measurable spaces within a dynamic matrix (Fig. 4F; tables S5 and S6).

To quantify the contribution of insufficient spatial resolution in obscuring the structure of ER tubular matrices, we compared cells in the absence of motion (i.e., in fixed cells) using three different imaging modalities of varying spatial resolution (diffraction-limited GI, 3D-SIM, or LLS-PAINT) (Fig. 4G). Predictably, improvements in spatial resolution decreased the measurable diameter of ER tubules (Fig. 4C; table S5 and S6). Moreover, imaging with diminishing spatial resolution limited the detectable degree of separation of tubules in a matrix (Fig. 4H; tables S5 and S6), decreasing their detectable density (Fig. 4I; tables S5 and S6). Thus, sufficient spatial and temporal resolution are both required to resolve the fine structure of tubular matrices in living cells, and with any imaging modality an apparently continuous structure may conceal spaces if they are beneath the resolvable power of the technique.

FIB-SEM reveals tubular matrices with heterogeneous topology

To overcome the limitations of optical microscopy in resolving the very fine structure of tubular matrices, we studied their morphology utilizing electron microscopy (EM). FIB-SEM was performed in native, untransfected cells to provide an additional

control against the possibility that overexpression of both Sec61β and ER3 coincidentally induce matrices. The conditions utilized for FIB-SEM were selected to result in 8 nm steps in *z* position (see Materials and Methods), which provides extremely high resolution in the *z* dimension and ensures that even thin structures like tubular matrices can be captured (Fig. 5A). This fine *z* resolution allowed the reconstruction of remarkably intricate three-dimensional tubular structures within even very thin sections of the cell (Fig. 5B, Movie 1). In contrast, we found that the topological complexity of matrices in the *z* dimension would be lost with diffraction-limited confocal imaging, as nearly the entire structure shown in Fig. 5B falls within the focal plane of a single confocal slice. Indeed, a projection of a theoretical confocal image derived from the EM data in Fig. 5B (see Materials and Methods) results in an image indistinguishable from an intact ER sheet (Fig. 5B, green footprint). In agreement with the LLS-PAINT data described previously, we find that these structures can contain substantial vertical topology even within a thin space, and a single slice through the structure often only reveals only a few isolated tubules (Fig. 5A). Inspection of the FIB-SEM data also revealed heterogeneity in matrix structures, from highly-convoluted three-dimensional structures to nearly planar arrays of tubes (e.g., Fig. 5, B versus C). Additionally, matrices can become incredibly tightly clustered, with spaces between tubules less than 50 nm (Fig. 5C). As such, it would be impossible to resolve these structures as distinct from sheets by SIM, and a challenge to do so even by LLS-PAINT.

Generally, areas of flat continuous membrane are described as having net zero curvature, while highly-curved regions of membrane have either net positive or negative curvature (*1*). In addition to the aforementioned tubular matrices, we also observe a number of structures in the ER that show local regions of near zero curvature in the ER membrane. The most dramatic of these regions are in true stacked ER sheets near the nucleus (Fig. 5D, cyan box), which have been described extensively (*16*). Of note, when imaged with diffraction-limited techniques these structures are nearly impossible to differentiate from tubular ER matrices (Fig. 5, D and E). We also observe that whenever stacked sheets are seen, they appear to be connected by membrane ‘ramps’ as previously described (*16*) and generally are close to the nucleus where the cell height is much greater than in the periphery (Fig. 5F, movie S5).

Localizing ER shaping proteins to tubular matrices

Given the highly-variable and complex nature of ER matrices identified in the FIB-SEM data, we speculated that examining the distribution of well-characterized ER-shaping proteins may provide insights into the diversity of these structures. Atlastin (ATL) GTPases have been well characterized as three-way junction-forming proteins localized within ER tubules, where they also bind ER-shaping reticulons (RTNs) (*17*, *18*). Thus, while they would not be expected to be enriched in sheets, they would be expected in matrices composed of densely-packed tubules and three-way junctions. We transfected COS-7 cells with HaloTag-ATL1 (one of three human ATL paralogs) and assessed the localization of ATL1 in live cells using diffraction-limited confocal microscopy (Fig. 6A). ATL1 was present in all structures classically considered as peripheral sheets. This was verified by immunostaining endogenous ATL3 in HeLa cells (Fig. 6B).

Interestingly, overexpression of ATLs has previously been shown to induce massive proliferation of "aberrant sheet-like structures" in a GTPase-dependent manner (*17*). This finding has been difficult to explain in light of the known role of ATL GTPases as mediators of three-way junction formation between tubules. We hypothesized that ATL overexpression might drive the formation of increasingly dense tubular matrices, which would appear as peripheral sheets using standard confocal imaging, due to insufficient spatiotemporal resolution. COS-7 cells coexpressing Sec61β and HaloTag-ATL1 were fixed and imaged using both diffraction-limited epifluorescence and 3D-SIM (Fig. 6C). Epifluorescence reveals the presence of peripheral sheet-like structures (Fig. 6Ci), as previously reported (*17*). However, the improved spatial resolution offered by 3D-SIM reveals these "aberrant sheet-like structures" to be dense tubular matrices (Fig. 6Cii). Crucially, these matrices contain ATL1 throughout (Fig. 6Ciii). These data collectively suggest that overexpression of ATLs does not drive formation of aberrant sheets but rather induces the formation of dense tubular matrices, consistent with the known cellular functions of ATLs.

We also looked at the distributions of other proteins associated with driving or stabilizing particular ER shapes. RTNs are a highly conserved family of ER proteins sharing significant sequence homology; multiple isoforms are present in most cell types and are typically associated with inducing and maintaining the curvature of the ER membrane in tubules (*3*). Classic work in the field has demonstrated localization of RTNs to tubular structures and their exclusion from sheet-like structures (*19*, *20*). Conversely, CLIMP63 is a traditional marker used to identify ER sheets, as it is believed to be involved in stabilizing the diameter of the ER lumen through interactions between long, dimeric coiled-coil domains (*2*). U-2 OS cells expressing Sec61β were stained with antibodies against endogenous CLIMP63 and RTN4A/B and imaged using Airyscan, a technique capable of achieving subdiffraction-limited imaging independent of SIM. In concordance with their tubular nature, many peripheral ER matrices are positive for RTN4A/B, and some of these are also enriched in CLIMP63 (Fig. 6D). There are also a smaller number of ER matrices that exclude RTN4A/B staining, as has been previously demonstrated in some peripheral sheet-like structures (*2*) (fig. S3). This complex heterogeneity in protein localization across matrices is unlikely to be a staining artifact, as overexpression of CLIMP63 or a variety of RTN isoforms also resulted in the presence of these proteins in some, but not all, ER matrices (fig. S3, see Supplementary Text for discussion). It is possible that heterogeneity in the distribution of these proteins is linked to the highly variable topologies shown in Fig. 5, which may correspond to functionally distinct classes of structures that appear identical when imaged with insufficient resolution.

To explore whether our observations hold true for multiple cell types, we examined the structure of the ER in three dimensions using either 3D-SIM or Airyscan in a variety of cell lines with highly variant morphology and diverse organisms/tissues of origin. In all ten cell lines examined, peripheral ER matrices were visible (Fig. 7). Although across cell types there seems to be significant variation in the topology, density, and cellular location of these structures, they are uniformly present and clearly visible using either of the two independent imaging techniques.

Discussion

Taken together, our data indicate that most previously described "sheet-like" ER structures within the thin periphery of cells are actually dense tubular matrices. Limitations in spatiotemporal resolution using conventional microscopy result in their appearance as continuous or fenestrated sheets. Additionally, we show a previously uncharacterized, rapidly dynamic state in the peripheral ER that is broadly dependent on cellular energy sources and that contributes to the misidentification of ER matrices in living cells.

The question therefore arises as to why the peripheral ER would be organized in this way. The structural conformation of tubular matrices is likely to be imperative to multiple features of ER biology, such as the ability of ER to rapidly alter its conformation in response to changing cellular needs. Interconversions among loose polygonal networks and dense matrices could be accomplished by simply sliding tubules along one another, rather than requiring energetically costly fusion or fission of ER membranes. This rapid interconversion between loose and tight polygonal arrays of tubules (e.g., movie S3) is likely to be important in enabling the ER to rapidly reconfigure its spatial footprint in response to intracellular structural rearrangements, cell shape changes, or during cell migration. Indeed, the ER and cytoskeleton co-exert a driving force for cytoplasmic streaming during cell expansion in *Arabidopsis*, and this is altered in mutants affecting ER morphology (*21*).

Clustering of tubules into tight arrays of three-way junctions might also function to decrease curvature stress across the ER, since the negative curvature of three-way junctions could help neutralize the positive curvature associated with tubules (*1*). Thus, a relatively planar network could be formed (e.g., Fig. 5C) in the thin periphery of cells, where a lack of vertical space might prevent the formation of stacked helicoidal sheets (*16*). Dense ER matrices are also predicted to have significantly greater membrane surface area than a flat sheet of similar dimensions, so they may allow storage of excess membrane proteins and lipids or provide increased surface for modulating lipid synthesis or protein folding. Such a tubular membrane reservoir may also be needed to facilitate the availability of ER membrane for modulating interactions with other organelles, such as mitochondria, lipid droplets, or endocytic compartments.

Our data do not conflict with the impressive literature describing the structures of flattened regions of ER associated with specialized functions, such as the nuclear envelope (*22*), helicoidal stacks in the perinuclear region (*16*), or flattened cisternal structures close to the plasma membrane (*23*). Rather, these structures represent one end of a spectrum of curvatures across the ER membrane, with the other end of the spectrum dominated by more prevalent ER tubules and the dense tubular matrices described in this paper.

The heterogeneity observed in fine ultrastructure and ER protein content also suggest that there may be several distinct types of ER matrices. It is possible, therefore, that these different structures may carry out distinct functions. For instance, our FIB-SEM data support previous three-dimensional EM reconstructions in suggesting that tubular morphology is far more heterogeneous than the cylindrical structures often depicted in models based on optical microscopy studies (*24*, *25*). Tubules can also take on flattened or highly irregular structures along their lengths, as has been described in ER contact sites with the plasma membrane (*23*). There is no reason to think that tubules within ER matrices could not also undergo these sorts of deformations, and as such ER

matrices close to the plasma membrane or other organelles (e.g., Fig. 3B) could potentially play important roles in rapidly facilitating calcium signaling or lipid transfer. These altered morphologies may also explain some of the variability in distribution of ER shaping proteins across matrices, as structures may become too dense or too deformed to stably hold certain classes of ER proteins, providing another mechanism for modulating peripheral ER function. It seems clear, in any event, that given the pathogenic role of impaired ER shaping and protein distribution in disorders such as the hereditary spastic paraplegias (*4*), the ER structure and dynamics described here will have important implications for understanding both basic cell biology and disease pathogenesis.

Acknowledgments: This work was supported by the Howard Hughes Medical Institute and the Intramural Research Programs of NINDS and NICHD, NIH. AVW was the recipient of a PRAT fellowship (NIGMS), and CJO was supported by an IARF fellowship from the NIH Office of AIDS Research. JN-A is supported by a UCL School of Pharmacy PhD studentship (to KH). JLS and CJO were additionally supported by a grant from the NIH Intramural AIDS Targeted Antiviral Program. DL is currently supported by National Key Research Program of China #2016YFA0500200. We wish to thank Helen White for assistance with cell culture, Lin Shao for assistance with imaging and data processing, Peng-Peng Zhu for advice on immunocytochemistry, and Riqiang Yan for his generous gift of an RTN4A/B antibody. Also, a special thanks to Erik Snapp for his provision of an MDCK ER-RFP stable cell line and his critical reading of the manuscript. The authors declare that there are no conflicts of interest. All data to support the conclusions are provided either in the manuscript or in the Supplementary Material.

References:

1. T. Shemesh *et al.*, A model for the generation and interconversion of ER morphologies. *Proc. Natl. Acad. Sci. U.S.A.* **111**, E5243–E5251 (2014).

2. Y. Shibata *et al.*, Mechanisms Determining the Morphology of the Peripheral ER. *Cell* **143**, 774–788 (2010).

3. U. Goyal, C. Blackstone, Untangling the web: mechanisms underlying ER network formation. *Biochim. Biophys. Acta* **1833**, 2492–2498 (2013).

4. C. Blackstone, Cellular pathways of hereditary spastic paraplegia. *Annu. Rev. Neurosci.* **35**, 25–47 (2012).

5. C. Lee, L. B. Chen, Dynamic behavior of endoplasmic reticulum in living cells. *Cell* **54**, 37–46 (1988).

6. A. R. English, G. K. Voeltz, Rab10 GTPase regulates ER dynamics and morphology. *Nat. Cell Biol*. **15**, 169–178 (2013).

7. D. Li *et al.*, Extended-resolution structured illumination imaging of endocytic and cytoskeletal dynamics. *Science* **349**, aab3500 (2015).

8. I. Arganda-Carreras, R. Fernández-González, A. Muñoz-Barrutia, C. Ortiz-De-Solorzano, 3D reconstruction of histological sections: Application to mammary gland tissue. *Microsc. Res. Tech.* **73**, 1019–1029 (2010).

9. S. Chen *et al.*, Lunapark stabilizes nascent three-way junctions in the endoplasmic reticulum. *Proc. Natl. Acad. Sci. U.S.A*. **112**, 418–423 (2015).

10. R. Metzler, J. Klafter, The random walk's guide to anomalous diffusion: a fractional dynamics approach. *Physics Reports* **339**, 1–77 (2000).

11. M. Guo *et al.*, Probing the stochastic, motor-driven properties of the cytoplasm using force spectrum microscopy. *Cell* **158**, 822–832 (2014).

12. C. Kural *et al.*, Tracking melanosomes inside a cell to study molecular motors and their interaction. *Proc. Natl. Acad. Sci. U.S.A*. **104**, 5378–5382 (2007).

13. K. Jaqaman *et al.*, Robust single-particle tracking in live-cell time-lapse sequences. *Nat. Meth*. **5**, 695–702 (2008).

14. W. R. Legant *et al.*, High-density three-dimensional localization microscopy across large volumes. *Nat. Meth*. **13**, 359–365 (2016).

15. B.-C. Chen *et al.*, Lattice light-sheet microscopy: Imaging molecules to embryos at high spatiotemporal resolution. *Science* **346**, 1257998 (2014).

16. M. Terasaki *et al.*, Stacked endoplasmic reticulum sheets are connected by helicoidal membrane motifs. *Cell* **154**, 285–296 (2013).

17. J. Hu *et al.*, A class of dynamin-like GTPases involved in the generation of the tubular ER network. *Cell* **138**, 549–561 (2009).

18. G. Orso *et al.*, Homotypic fusion of ER membranes requires the dynamin-like GTPase Atlastin. *Nature* **460**, 978–983 (2009).

19. G. K. Voeltz, W. A. Prinz, Y. Shibata, J. M. Rist, T. A. Rapoport, A class of membrane proteins shaping the tubular endoplasmic reticulum. *Cell* **124**, 573–586 (2006).

20. Y. Shibata *et al.*, The reticulon and DP1/Yop1p proteins form immobile oligomers in the tubular endoplasmic reticulum. *J. Biol. Chem.* **283**, 18892–18904 (2008).

21. G. Stefano, L. Renna, F. Brandizzi, The endoplasmic reticulum exerts control over organelle streaming during cell expansion. *J. Cell Sci*. **127**, 947–953 (2014).

22. M. W. Hetzer, The nuclear envelope. *Cold Spring Harb. Perspect. Biol*. **2**,

a000539 (2010).

23. R. Fernández-Busnadiego, Y. Saheki, P. De Camilli, Three-dimensional architecture of extended synaptotagmin-mediated endoplasmic reticulum-plasma membrane contact sites. *Proc. Natl. Acad. Sci. U.S.A.* **112**, E2004–2013 (2015).

24. M. Puhka, M. Joensuu, H. Vihinen, I. Belevich, E. Jokitalo, Progressive sheet-to-tubule transformation is a general mechanism for endoplasmic reticulum partitioning in dividing mammalian cells. *Mol. Biol. Cell*. **23**, 2424–2432 (2012).

25. M. Puhka, H. Vihinen, M. Joensuu, E. Jokitalo, Endoplasmic reticulum remains continuous and undergoes sheet-to-tubule transformation during cell division in mammalian cells. *J. Cell Biol*. **179**, 895–909 (2007).

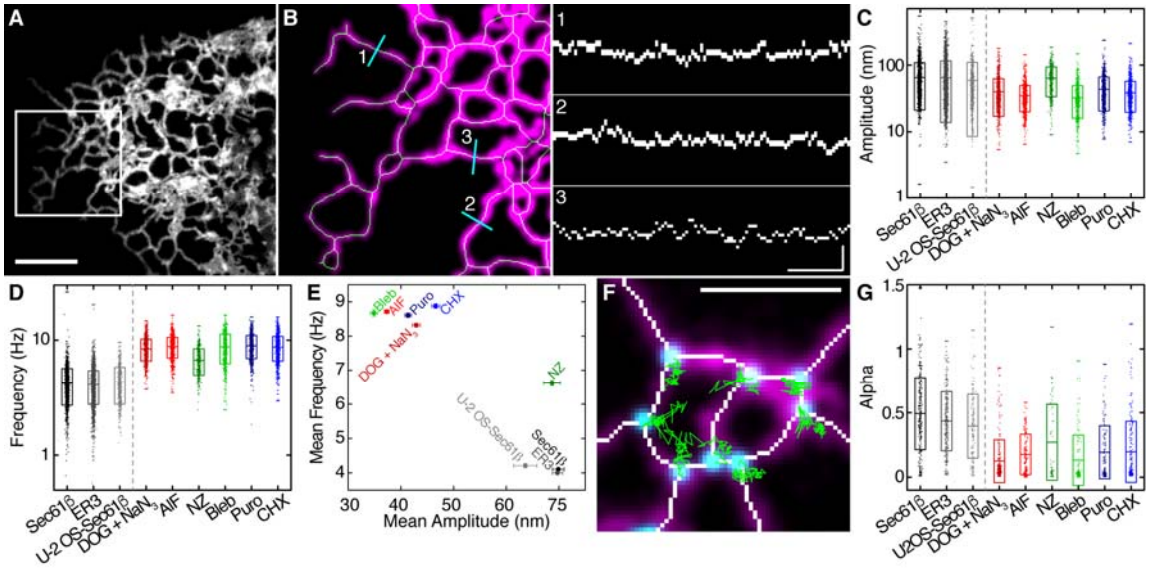

Fig. 1. The Peripheral ER moves at high speeds. (A) Tubular ER in the periphery of a COS-7 cell expressing mEmerald-Sec61β imaged live at 40 Hz using GI-SIM microscopy. Scale bar, 2 μm. **(B)** ER tubules within the boxed region in (A), identified using a skeletonization algorithm; the midline of each tubule (green) is mapped onto the fluorescence (magenta; left panel). Position of the midlines are plotted as kymographs against time for each of the three locations shown in cyan (right panels). Scale bars, 200 nm and 0.5 s. **(C** and **D)** The amplitudes (C) and frequencies (D) of tubular ER oscillations in COS-7 cells expressing mEmerald-Sec61β treated with deoxyglucose plus sodium azide (DOG + NaN_3), aluminum fluoride (AlF), nocodazole (NZ), blebbistatin (Bleb), puromycin (Puro) and cycloheximide (CHX). Untreated controls using a luminal ER marker (ER3) and results for a different cell line (U-2 OS-Sec61β) are also shown. **(E)** Plot of frequency versus amplitude for tubular oscillations in treated and untreated cells. **(F)** Locations of three-way junctions derived from skeletonized data (white). Original fluorescence is shown in magenta, while example tracks of junctions (cyan) over 2.5 s are indicated in green. Scale bar, 2 μm. **(G)** MSD scaling exponent (α values) for treated and control cells. See tables S1 and S2 for a detailed list of means and test statistics.

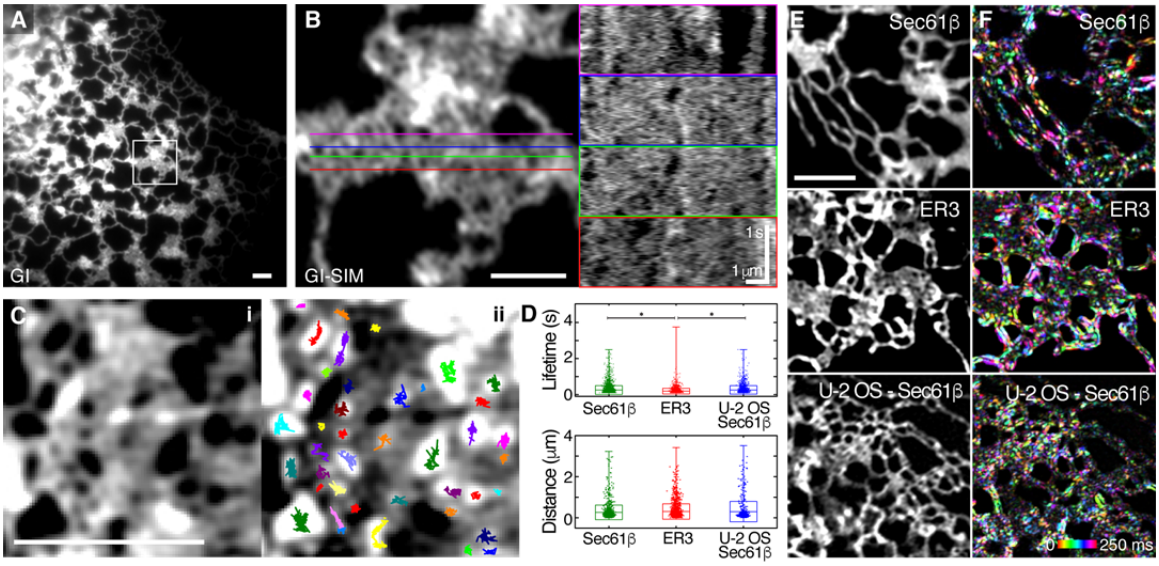

Fig. 2. Peripheral ER "sheets" are highly dynamic and riddled with spaces. (A) COS-7 cell expressing mEmerald-Sec61β imaged live at 40 Hz using GI exhibits many peripheral sheet-like structures. **(B)** GI-SIM of the boxed region in (A) showing many discrete spaces throughout the structure (left panel). Colored lines correspond to the locations of the kymographs shown in the right hand panel. Voids in intensity within the structure can be seen appearing and disappearing over time. **(C)** Single particle tracking (SPT) of dark spaces within the structure. The fluorescence image **(i)** was inverted, and spaces were tracked using SPT algorithms. Tracks overlaid onto the inverted image are shown in **(ii)**, with trajectories shown in different colors. **(D)** Each track length corresponds to the lifetime of the space, with distance across the space, or rather the distance between tubules, is also quantified. The asterisks denote significant difference between means, detailed in Table S4. **(E** and **F)** Temporal intensity derivative analysis (see Materials and Methods) of representative peripheral sheet-like structures in a COS-7 cell expressing mEmerald-Sec61β, with a luminal ER marker (ER3) and another cell line (U-2 OS-Sec61β) as controls. **(E)** Original fluorescence image. **(F)** Each consecutive frame over a 250 ms time period is color-coded, with intensity corresponding to the magnitude of fluorescence change. Scale bars, 2 µm. See tables S3 and S4 for a detailed list of means and test statistics.

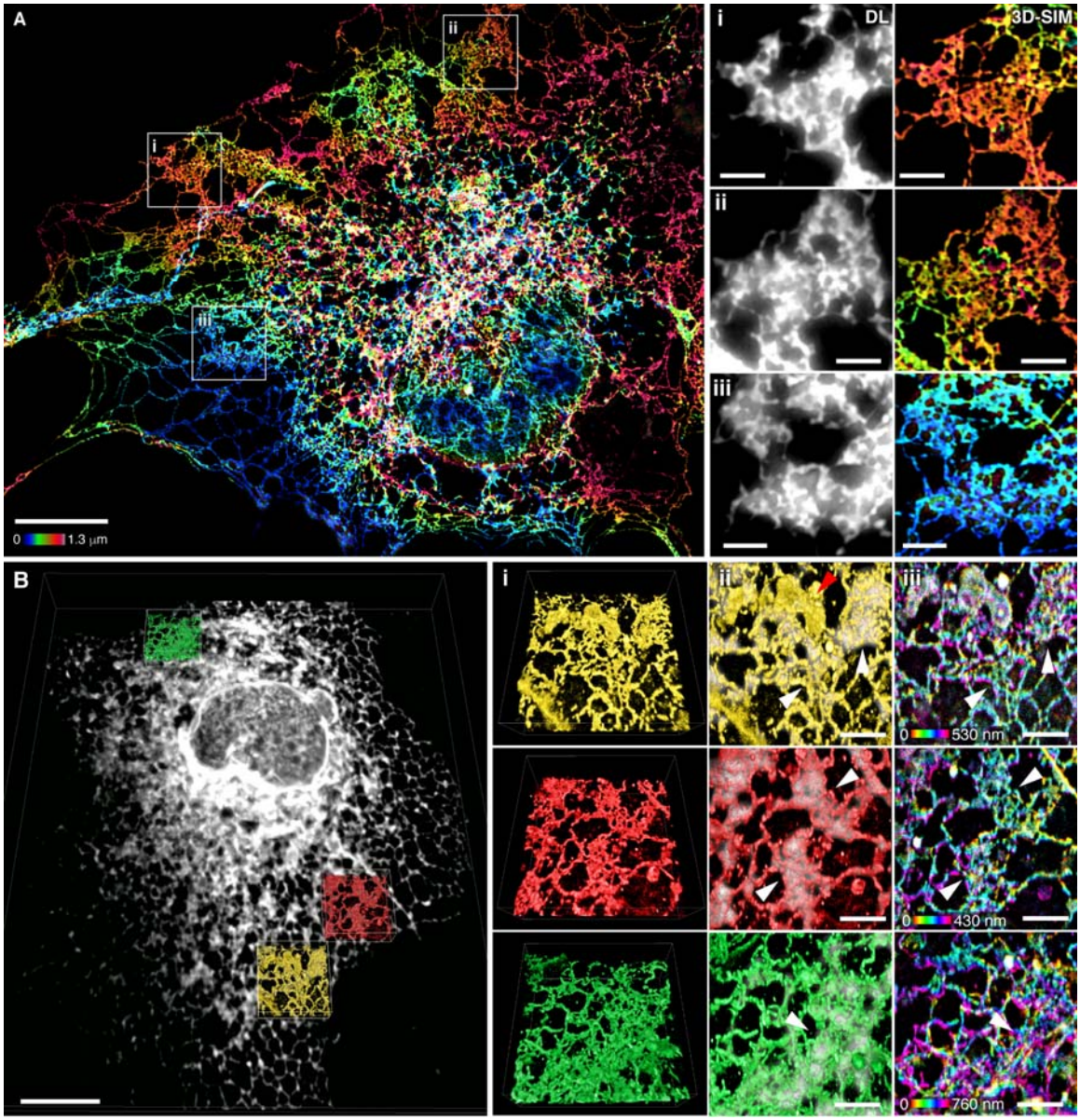

Fig. 3. Many peripheral structures classically identified as sheets are instead dense matrices of tubules. **(A)** Fixed COS-7 cell expressing mEmerald-Sec61β imaged by 3D-SIM and color coded by *z* position (left panel). Scale bar, 10 µm. Magnified regions **(i-iii)** illustrate dense tubular matrices (right panels) which appear as sheets by diffraction-limited (DL) epifluorescence (left panels). Scale bars, 2 µm. **(B)** Deconvolved, diffraction-limited LLS imaging of a fixed COS-7 cell overexpressing mEmerald-Sec61β (gray). All internal lipid membranes were reconstructed using LLS-PAINT microscopy. Data from three regions containing ER matrices are shown in colored insets. Scale bar, 10 µm. The three boxed regions are enlarged (right panels). **(i)** 3D orientation of LLS-PAINT volume rendering, **(ii)** overlay of LLS-PAINT and diffraction-limited LLS imaging volume rendering (gray), and **(iii)** LLS-PAINT color coded by *z* position. White arrows mark areas which appear as sheets by diffraction-limited imaging, and the red

arrow (top of (ii)) denotes a mitochondrion. Scale bars, 2 μm.

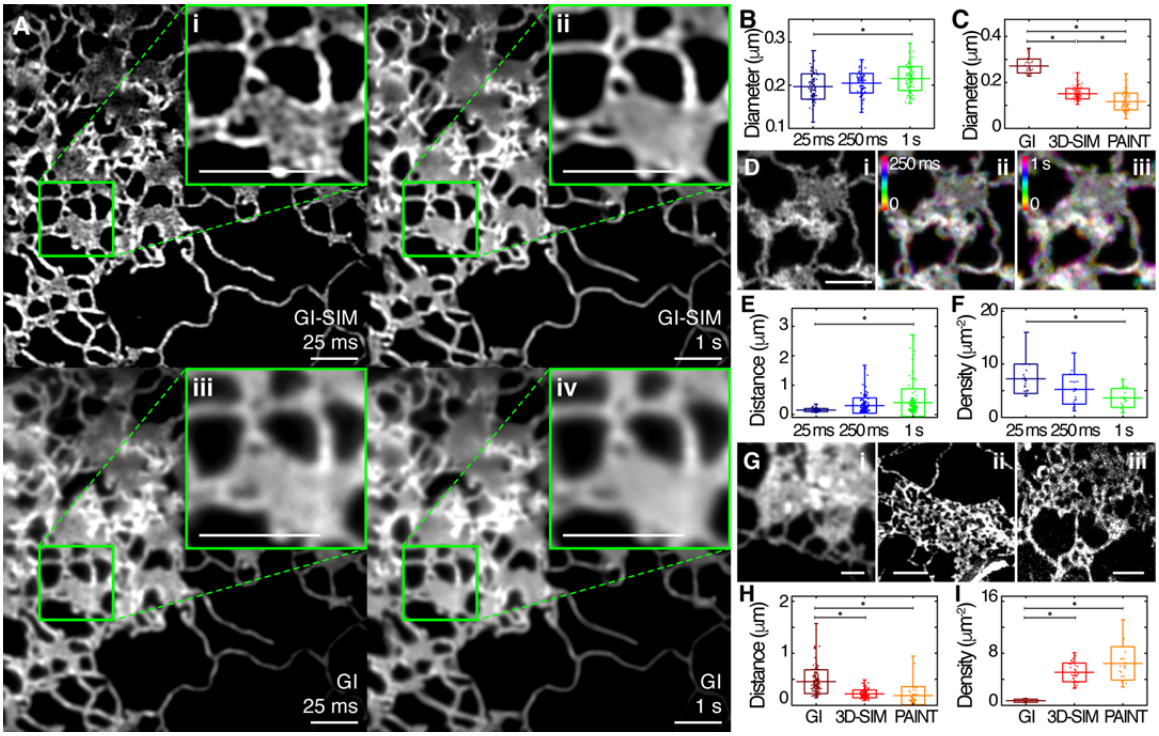

Fig. 4. Effects of spatiotemporal blurring on imaging ER tubular matrices. (A) A COS-7 cell expressing mEmerald-Sec61β, imaged live using GI-SIM, showing both single 25 ms frames **(i, iii)** and 40 frames averaged over 1 s **(ii, iv)**. The top row shows the GI-SIM images while the bottom row shows the corresponding diffraction-limited images with GI illumination, demonstrating the combined effects of spatial and temporal limitations in resolution. **(B** and **C)** The measurable diameter of isolated ER tubules found outside of matrices also decreases with increasing temporal (B) and spatial (C) resolution. **(D)** Structure of a representative tubular ER matrix imaged in a live cell using GI-SIM when integrating image frames for 25 ms (1 frame), 250 ms (10 frames), or 1 s (40 frames) as in (A). **(E** and **F)** Quantification of the measurable distance between tubules (E), and density of these spaces (F) within tubular matrices for each functional exposure time. **(G)** Representative images of tubular matrices imaged in fixed cells by diffraction-limited GI **(i)**, 3D-SIM **(ii)**, and LLS-PAINT **(iii)**. **(H** and **I)** Quantification of the measurable distance between tubules (H), and density of these spaces (I) in tubular matrices, as identified by imaging modalities of increasing spatial resolution. Scale bars, 2 μm. See table S5 and S6 for a detailed list of means and test statistics.

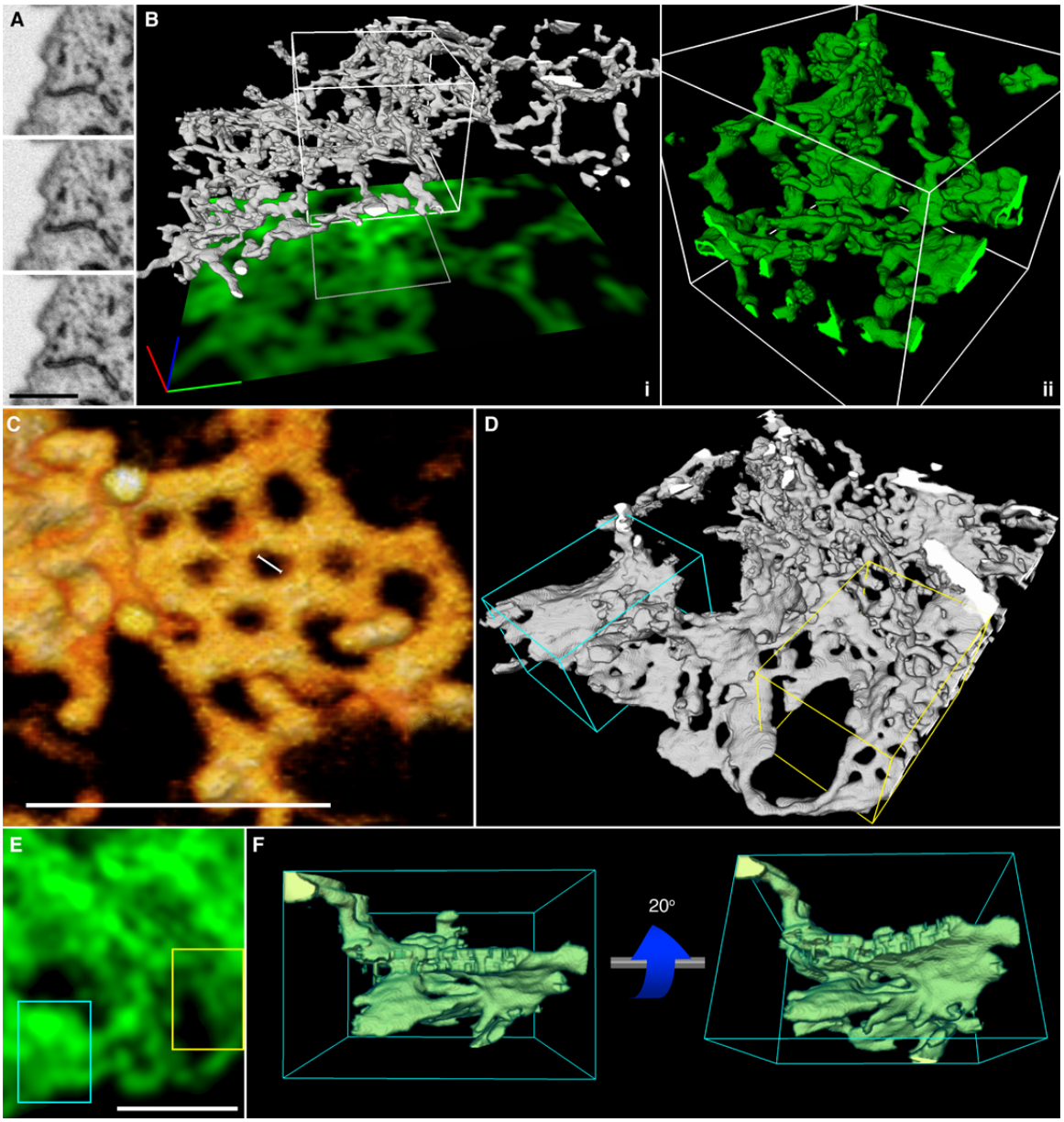

Fig. 5. ER tubules form highly convoluted and intricate structures within the resolvable volume limits of any optical imaging technique. (A) Three consecutive FIB-SEM slices through an ER matrix spaced by 8 nm. Scale bar is 1 μm. **(B)** Three-dimensional reconstruction of a tubular matrix in a thin section (~ 600 -1200 nm between the plasma membranes) of the cell. **(i)** The footprint shows the theoretically highest resolution that could be achieved with a single confocal slice through the structure directly shown above. Three-dimensional scale bar displays 1 μm in each direction. **(ii)** Zoom of the reconstruction of boxed region in (i). **(C)** 3D rendering of raw EM data showing an example of an approximately planar ER matrix with sub-resolution spaces (large scale bar, 500 nm; small scale bar, 50 nm). **(D)** 3D rendering of the ER at the border of perinuclear and peripheral regions of the cell, showing both stacked helicoidal sheets (cyan box) and ER matrices (yellow box). **(E)** A theoretical confocal image of the structure, showing the difficulty in distinguishing these structures by diffraction-limited

imaging. **(F)** Views from the side of a stacked helicoidal sheet in the perinuclear region of the ER (from Cyan box in (D)), showing the pitch of the intact membranes.

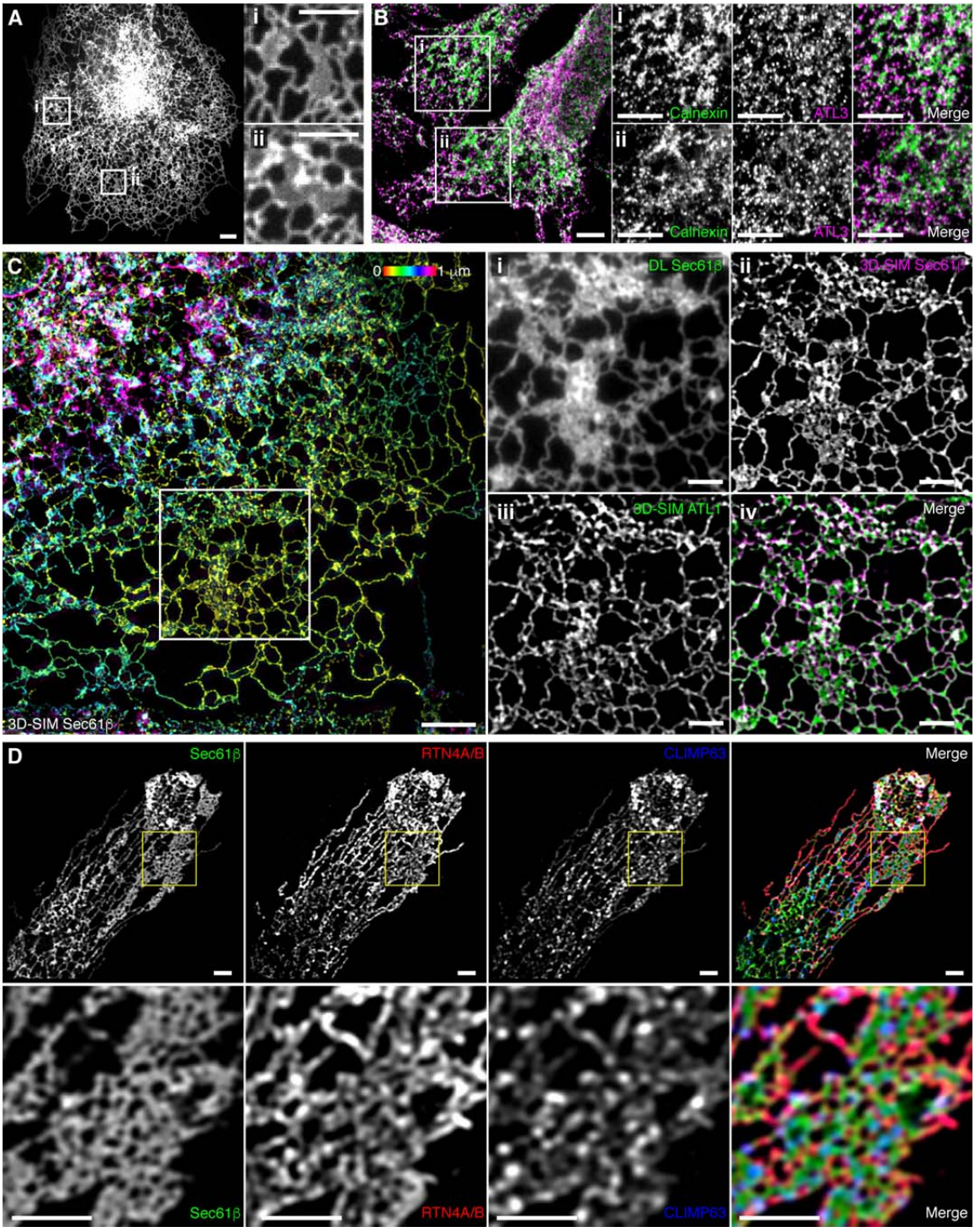

Fig. 6. Localization of ER-shaping proteins within dense tubular matrices. (A) COS-7 cell expressing low levels of HaloTag-ATL1 imaged live with conventional spinning disk microscopy. Inset panels **(i)** and **(ii)** demonstrate ATL1 localization throughout structures that appear to be peripheral sheets by spatiotemporally-limited imaging techniques. **(B)** Merged image of a fixed HeLa cell stained for the endogenous ER marker calnexin (left inset panels), endogenous ATL3 (middle inset panels), and merged

image (right inset panels) acquired with conventional scanning point confocal microscopy. The two insets, **(i)** and **(ii),** show endogenous ATL3 localization to structures that appear as sheets. **(C)** A Fixed COS-7 cell expressing mEmerald-Sec61β and HaloTag-ATL1 imaged by WF-SIM. mEmerald-Sec61β fluorescence is color coded by *z* position. Structures that appear as sheets by diffraction limited imaging **(i)**, are revealed to be dense tubular matrices **(ii)** that are positive for ATL1 **(iii)**; the merged image of (ii) and (iii) is in **(iv)**. **(D)** U-2 OS cell expressing mEmerald-Sec61β stained for endogenous RTN4A/B and CLIMP63 with the boxed region magnified (bottom row), illustrating localizations of both proteins within a tubular matrix. Merged images are at the far right. Scale bars, 2 μm.

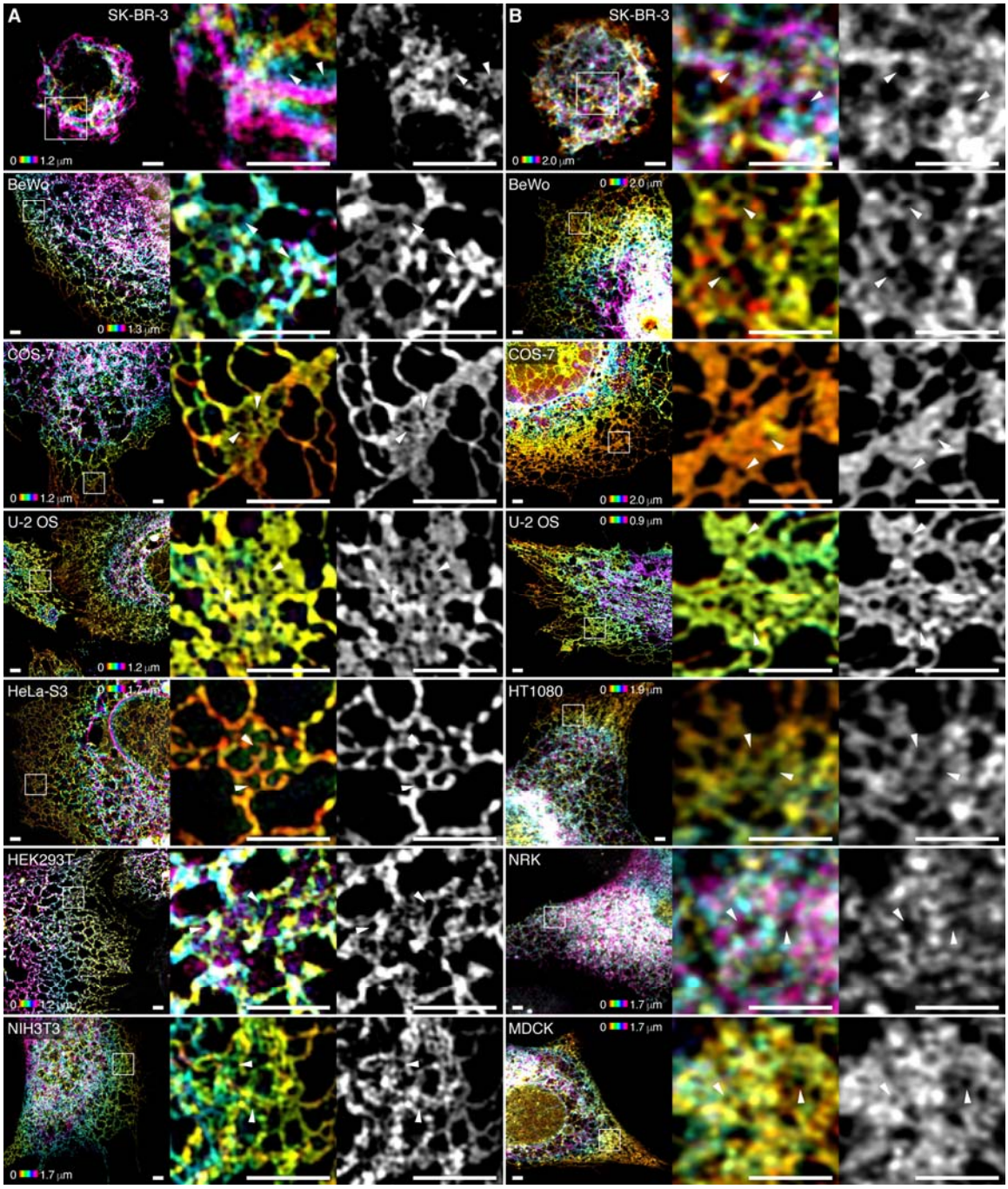

Fig. 7. Tubular ER matrices are present in different cell types. (**A** and **B**) Various cell lines expressing mEmerald-Sec61β were imaged using 3D-SIM (A) or, where fluorescence intensity was insufficient, Airyscan (B). The first four cell lines were imaged using both modalities, demonstrating that the dense matrix structures are not artifacts of any given imaging modality. Boxed regions highlighting representative tubular ER matrices in each cell type are magnified to the right. White arrows indicate subdiffraction-limited spaces between tubules. Scale bars, 2 µm. The signal of mEmerald-Sec61β fluorescence is color coded by *z* position in the two left panels.

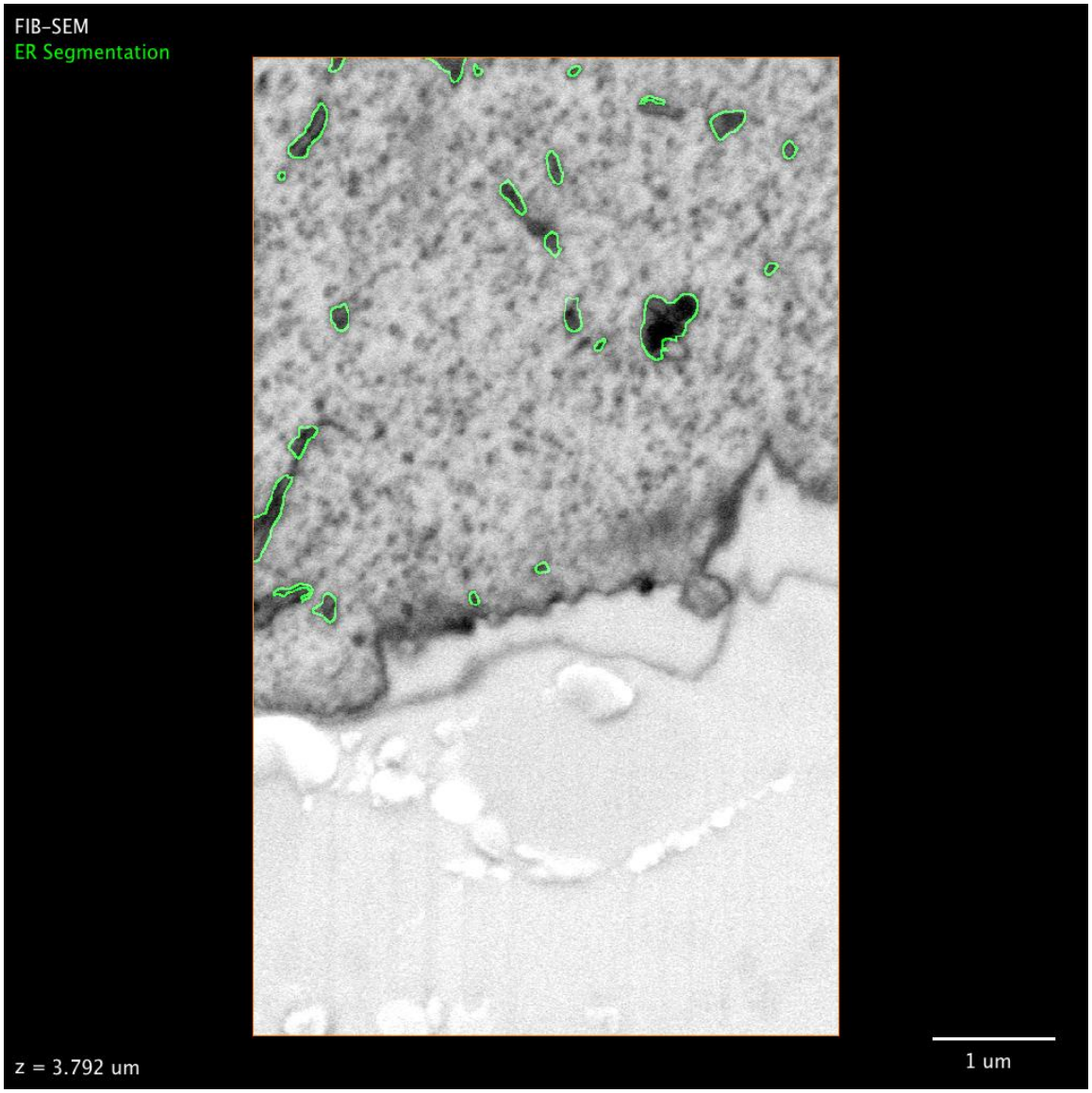

Movie 1. **Three dimensional reconstruction of FIB-SEM data reveals a convoluted ER matrix.** Raw two-dimensional FIB-SEM data of ER tubules. The ER is segmented in green, and the three dimensional reconstruction is shown, revealing an ER matrix. When confocal resolution is simulated, the convoluted nature of the structure is masked.

Supplementary Materials for

Increased spatiotemporal resolution reveals highly dynamic dense tubular matrices in the peripheral ER

Jonathon Nixon-Abell, Christopher J. Obara, Aubrey V. Weigel, Dong Li, Wesley R. Legant, C. Shan Xu, H. Amalia Pasolli, Kirsten Harvey, Harald F. Hess, Eric Betzig, Craig Blackstone*, Jennifer Lippincott-Schwartz*

*correspondence to: blackstc@ninds.nih.gov, lippincottschwartzj@janelia.hhmi.org

This PDF file includes:

Other Supplementary Materials for this manuscript includes the following:

Materials and Methods

Plasmids and Antibodies

Constructs expressing Myc- and HA-tagged atlastins have been previously described (*1*), with HaloTag-ATL1 purchased from Promega. Constructs expressing mEmerald-Sec61β and mApple-Sec61β were generated by replacing the GFP cassette of pAcGFP1-Sec61β (*2*) with corresponding fluorescent proteins, using flanking *Age*I and *Bsr*G1 restriction sites. Reticulon constructs were cloned from whole brain cDNA and inserted into pmCherry-C1 using the *Bgl*II and *Sal*I restriction sites. Lifeact-mApple has been previously described (*3*), and mEmerald-ER-3 (ER3) was a gift from Michael Davidson (Addgene plasmid # 54082). ER3 consists of an ER lumen-targeting motif fused to mEmerald with a C-terminal KDEL tag.

Commercially available mouse monoclonal anti-Myc epitope (1:200; IgG_1, clone 9E10; Santa Cruz Biotechnology) and rabbit polyclonal anti-HA epitope (1:200; IgG, clone Y-11; Santa Cruz Biotechnology) antibodies were used for Immunocytochemistry. In addition, a custom affinity-purified mouse monoclonal anti-ATL3 (No. 6115, IgG, clone 9H2B12; residues 561–578; acetyl-CATVRDAVVGRPSMDKKAQ-OH) antibody was used at 1:100. The anti-RTN4A/B antibody was a kind gift from Riqiang Yan, and was used as described previously (*4*). CLIMP63 was stained using a commercial antibody purchased from Enzo Lifesciences (1:250; IgG_{2a}, clone G1/296).

Cell Culture, Transfection, and Plating

COS-7, U-2 OS and HeLa cells (ATCC) were grown in phenol red-free Dulbecco's Modified Eagle Medium (DMEM) supplemented with 10% (v/v) FBS (Corning), 2 mM L-glutamine and 100 U/ml penicillin and 100 μg/ml streptomycin at 37°C and 5% CO_2. MDCK cells were a line stably expressing ER-RFP (*5*, *6*) generously provided by Erik Snapp. All other cells (SK-BR-3, BeWo, HeLa-S3, HEK293T, HT1080, NRK and NIH3T3) were grown according to manufacturer's specifications (ATCC).

Coverslips and chambers were pre-coated with 400-600 μg/ml Matrigel (Corning), and cells were seeded to achieve ~60% confluency at the time of imaging. Transfections were executed using Lipofectamine 3000 (Thermo Fisher Scientific) according to the manufacturer's specifications. Fluorescently-tagged Sec61β alone was transfected at 1 μg/ 35 mm chamber, or else cotransfected at a ~3-4:1 ratio with the alternate plasmid. Imaging was performed between 14-22 h post-transfection. Where indicated, HaloTag-ATL1 was labeled with JF549 as previously described (*7*), and cells were imaged immediately post-labeling.

Drug Treatments

All drugs used in the paper were purchased from Sigma Aldrich and used as has been described (*8*). Drugs were diluted from high concentration stocks reconstituted in DMSO, and diluted to the appropriate concentration in complete medium unless otherwise indicated. Cycloheximide (CHX) and Puromycin (Puro) were used at a final concentration of 100 μg/ml, Nocodazole (NZ) was used at 30 μM, and Blebbistatin (Bleb) was used at a final concentration of 50 μM. ATP depletion was accomplished by incubating the cells for one hour in 10 mM 2-deoxyglucose (DOG) and 2 mM sodium azide (NaN_3) in PBS at 37 °C, and AlF treatment was performed as previously described

(*9*) in HBSS. HBSS-only controls were also run for all experiments using AlF, and no difference in any phenotype studied was seen compared to untreated controls (data not shown).

Immunocytochemistry

For immunocytochemistry staining, cells were seeded into No. 1.5 imaging chambers (Lab-Tek) coated with Matrigel, and then fixed with 4% (w/v) paraformaldehyde (PFA) for 20 min at room temperature (RT). Cells were then permeabilized with 0.2% (w/v) saponin (Sigma-Aldrich) for 30 min, and blocked in 5% (v/v) donkey serum (Sigma-Aldrich) doped with 0.05% (w/v) saponin for 1 h at RT. Primary antibodies were diluted in block to the aforementioned concentrations, added to samples, and incubated overnight at 4°C. Secondary anti-mouse and anti-rabbit antibodies conjugated to Alexa 488, Alexa 555 (1:1000; Life Technologies) were made in block and incubated with samples for 30 min at RT. Imaging was performed in clean PBS.

Confocal Microscopy

Live-cell confocal imaging was performed using a customized Nikon TiE inverted scope outfitted with a Yokogawa spinning-disk scan head (#CSU-X1, Yokogawa) and a Photometrics EM-CCD camera (Evolve 512) with 500 ms exposure time. Fluorescence was collected using a 60× Plan-Apochromat 1.40 NA oil objective (Nikon) with the additional use of a 1.5× optovar to create a final pixel size of 130 nm. Cells were imaged in DMEM and incubated with a LiveCell Imaging Chamber (Nikon) at 37°C and 5% CO_2.

Fixed-cell confocal microscopy was performed using a Zeiss 780 laser scanning confocal microscope equipped with a 32-channel multi-anode spectral detector. Excitations were performed sequentially using 405, 488, 561, or 633 nm lines as needed, and imaging conditions were experimentally selected to minimize crosstalk. The resulting fluorescence was collected using a 100× Plan-Apochromat 1.4 NA oil objective (Carl Zeiss) and images were prepared using the commercial Zen software package (Carl Zeiss).

Airyscan imaging was performed in fixed cells using a Zeiss 880 outfitted with an Airyscan module. Cells were seeded onto matrigel-coated coverslips, fixed in 4% (w/v) PFA supplemented with 0.2% (w/v) glutaraldehyde at RT for 20 min. After fixation, cells were washed in RT PBS and imaged in clean PBS. Data was collected using a 63x 1.4 NA objective and immersion oil optimized for 30 °C (Carl Zeiss). Colors were collected sequentially to minimize crosstalk, and Airyscan processing was performed using the Airyscan module in the commercial ZEN software package (Carl Zeiss).

Structured Illumination Microscopy (SIM)

Fixed cell, 3D-SIM was performed using a commercial Zeiss microscope (ELYRA SR-SIM, Carl Zeiss Microimaging) outfitted with a Plan-Aprochromat 63× 1.4 NA objective lens. Samples were fixed in 4% PFA supplemented with 0.1% glutaraldehyde at RT for 20 min. Cells were imaged in PBS at RT with a final pixel size of 40 nm and 110 nm *z* plane spacing using three rotations of the SIM grating. SIM processing was performed using the SIM module in the Zen software package (Carl Zeiss

Microimaging), and multicolor images were channel aligned using a matrix generated with Tetraspeck beads (Life Technologies) imaged on the same day as the cells.

Grazing Incidence-Structured Illumination Microscopy (GI-SIM)

GI-SIM was performed in a high speed SIM microscope previously adapted for total internal reflection fluorescence (TIRF)-SIM (*10*). GI-SIM shared the same beam path configuration as the high-speed TIRF-SIM system. In TIRF illumination mode, because the intensity of evanescent wave of excitation light exponentially decayed from the interface between cover slip and cell sample, the characteristic penetration depth of the evanescent wave limited the TIRF-SIM imaging depth to around 100 nm (*11*), in which much of the ER network lies outside. In order to increase the imaging depth, it is straightforward to tune down the incident angle that is inversely proportional to the penetration depth of the evanescent wave (*11*). We realized that when the incident angle was tuned to slightly smaller than the critical angle, where the refraction angle at the interface was near 90 degrees, and the refracted light grazed the surface of the cover slip, the grazing incident light actually formed a thin light sheet parallel to the cover slip surface. The thin light sheet intensity remained constant in both lateral and axial directions, and its thickness could be adjusted by tuning the incident angle of excitation light. The optimum thickness of grazing incident light sheet should match the depth-of-focus of the high NA objective (Zeiss alpha Plan-Apochromat 100x/1.57 Oil-HI), which is around 700 nm. To implement GI-SIM, we used the grating pattern generation algorithm previously developed for patterned activation nonlinear SIM. It permitted us to finely tune the incident angle of excitation light, i.e. the period of illumination pattern (*10*). We identified the optimum incident angle by keeping the out-of-focus background of the TIRF image as little as possible, meanwhile observing as much ER structure as possible. After we identified the critical angle for grazing incidence, the raw image acquisition and SIM image reconstruction procedure is the same as TIRF-SIM (*10*). Time-lapse images were also subject to a traditional bleach correction algorithm by histogram matching in ImageJ (NIH). Cells were plated and transfected on Matrigel-coated high-NA coverslips (Zeiss) and imaging was performed the following day.

Lattice Light Sheet-Point Accumulation for Imaging in Nanoscale Topography (LLS-PAINT)

LLS-PAINT was performed as described elsewhere (*12*) using a custom built Lattice Light Sheet microscope (*13*). Membrane labeling was performed sequentially with BODIPY-TR (LifeTechnologies) followed by AZEP-Rh (*7*) to label intracellular membranes and carried out over 14 days total. The final image was reconstructed from 548,792,627 individual molecular localizations with a median precision of 7.2 nm laterally and 41.0 nm axially. Immediately prior to PAINT imaging, a diffraction limited dithered LLS image of mEmerald-Sec61β was taken for comparison in the same cell.

Electron Microscopy (EM)

In preparation for EM, cells were grown in 100 mm culture dishes (Corning) in standard cell culture conditions. Cells were fixed in 2% (w/v) glutaraldehyde in 0.08 M cacodylate buffer for one hour. Cells were then post-fixed with osmium according to a modified ROTO (reduced osmium thiocarbohydrazide-osmium) protocol (*14*). Briefly,

fixation was performed in 1% (w/v) OsO_4 in 0.1 M cacodylate buffer for 30 min on ice, followed by a wash in cacodylate buffer. The cells were then incubated with 1% (w/v) thiocarbohydrazide in water for 10 minutes at room temperature, followed by immersion in 1% (w/v) OsO_4 in 0.1 M cacodylate for 30 minutes at 4°C. Cells were contrasted en bloc with 1% (v/v) uranyl acetate, dehydrated in ethanol, and embedded in Durcupan ACM (Fluka). FIB-SEM was performed using a Zeiss NVision40 Focused Ion Beam Scanning Electron Microscope. SEM and FIB milling steps were optimized to produce isotropic 8 nm voxels. The SEM image stack was acquired at 300 kHz/voxel using a 3-nA electron beam at 1.5 kV landing energy for imaging and a 30-kV gallium ion beam for FIB milling.

Structured Illumination Microscopy Reconstruction and Fourier Filtering

SIM reconstruction was performed utilizing a modified reconstruction algorithm based on the previously described Gustafsson algorithm (*15*). During reconstruction, data was filtered in Fourier space using a variety of filters to minimize the appearance of reconstruction artifacts. This included at least a one log scan of the Wiener filter and a variety of suppression radii around the peaks at Abbe's limit (fig. S4), in addition to a variety of apodization functions designed to roll off the noise at the limit of resolution. While the first two filters were selected individually for each image, the apodization function was decided collectively for the data and applied to every image in the paper. The apodization function was a single Gaussian blur using a radius that is smaller than the resolution limit of the technique, $\sigma = 45$ nm in real space. This allows most SIM reconstruction artifacts to be filtered out, maximizing the potential signal to noise with only a small price in functional resolution (fig. S4).

Reconstruction of Three Dimensional EM Data

Three dimensional FIB-SEM data was reconstructed and the ER segmented using a pseudo-automated approach. First, images were prepped, cropped, and inverted using ImageJ, so that osmium signal appeared as fluorescence for subsequent analysis. Images were then loaded into Ilastik (*16*) for pixel classification. The pixel classification algorithm was used to generate a probability map for cellular membranes, based upon the osmium signal. A carving algorithm within Ilastik was then utilized. The resulting segmentation was overlaid onto the raw EM data using Amira (FEI) and quality checked by eye throughout each slice of the reconstruction. Simulation of serial section data was performed by simply summing the requisite number of FIB-SEM slices that would have been present in a single slice acquired by serial section.

Data Visualization

Two dimensional image preparation and analysis was generally performed using ImageJ (NIH), and three dimensional image preparation was performed using Amira (FEI).

Skeletonization

Skeletonization of images was performed using ImageJ (NIH). First, images were pre-processed using enhanced local contrast (CLAHE) to help flatten the intensity of the ER. The images were then manually thresholded, made binary, and skeletonized. Using

the AnalyzeSkeleton (*17*) plugin in ImageJ, branches and junctions were determined from the skeletonized images. In short, skeletonized pixels with exactly two neighbors are considered branches and pixels with more than two neighbors, junctions.

Analysis of Tubule Motion

After obtaining the skeletonized image, lines were drawn perpendicular to the skeletonized structure over a number of tubules that were to be analyzed. In order to avoid the confounding effects of junctions crossing the line, lines were placed on sections of tubule that were spatially separated from any junctions. Kymographs of the skeletonized data were then generated along the lines over a total time lapse of 100 frames (2.5 s) (see Fig. 1B, for example). Amplitude was extracted from the kymograph by using a custom written peak finding algorithm in Labview, then measuring the distance between the maximum and minimum of peaks of the skeleton during the kymograph's time window. The frequency was defined as the inverse of the period, which was measured by dividing the length of the time course by the number of paired maxima and minima within the data.

Junction Tracking

Junctions were determined directly from the AnalyzeSkeleton plugin in ImageJ. Junctions from the tagged skeleton output of the AnalyzeSkeleton plugin typically occupy 1-5 pixels. The binary junction images were smoothed with a Gaussian kernel having a standard deviation of 1.0 pixel, resulting in single-particle-like images. The resulting images were then fed directly into the u-track SPT software (*18*).

Mean Square Displacement Analysis

Trajectories, with a lifetime of at least 10 frames (0.25 s) were obtained. The trajectories were characterized through their mean square displacement (MSD). $MSD = (1/T)\sum_{t=1}^{T}(r(t) - r_0)^2$, where T is the total movie time and r the displacement. The MSD can be described as MSD ~ t^{α} where α can be used to describe a particle's motion as Brownian ($\alpha = 1$), subdiffusive ($\alpha < 1$), or superdiffusive ($\alpha > 1$) (*19*).

Kymographs

Kymographs were prepared from time lapse images by manually drawing lines across the image and using the standard reslice package in ImageJ. The resulting figure represents the intensity by pixel along the line graphed against time. Axes are labeled to indicate the respective x (μm) and t (s).

Tracking Spaces in Sheets

GI-SIM images of the ER were cropped such that the ROI was an individual sheet. The area outside of the sheet was then subtracted and the intensity of the images inverted. The transformation resulted in local intensity minima (spaces) becoming local intensity maxima. These maxima were then directly entered into the u-track SPT algorithm.

Space Lifetime & Density

Track length corresponds to the lifetime of the spaces. To account for clipping of lifetimes at either the start or end of the movie, the distribution of lifetimes was corrected

following Loerke and colleagues (*20*, *21*). To measure the density of spaces, the area of each sheet was measured by drawing a freehand ROI around the sheet and then measuring the area of the ROI in ImageJ. The density of spaces was then calculated as the number of spaces within the sheet divided by the area of that particular sheet.

Temporal Intensity Derivative

The derivative was calculated by choosing a defined region and time series of interest and processing the data as described for GI-SIM (fig. S1A). Each frame of the time-lapse image was then subtracted pixel by pixel from the following frame using a floating 32-bit depth pixel to ensure negative signals were not lost (fig. S1B). The resulting image was squared on a per-pixel basis, to make all changes positive integers (fig. S1C). The upper limit of the dynamic range was reset to the theoretical maximum in order to normalize the derivative between samples. The resulting time-lapse image was temporally color coded, yielding a spatial map of the change in fluorescence intensity over time (fig. S1D).

Measuring the Diameter of Tubules and Spaces in Matrices

The size of apparent spaces within tubular matrices was measured by fitting the intensity cross-section profile of each minima to a Gaussian curve. The full width at half-maximum of the Gaussian curves provides a good estimate of the distance across the space. The diameter of tubules was measured in a similar fashion: intensity cross-sections along several locations of tubules were fit to a Gaussian curve and the full width at half-maximum was reported as the diameter of the tubule.

Temporal Blurring

To simulate the effects of longer exposure times in GI-SIM, the appropriate number of SIM frames collected at 40 Hz were merged using a simple sum projection in ImageJ. Thus, 250 ms images are the sum of 10 individual 25 ms frames, and 1 s images are the sum of 40 separate 25 ms frames. When color-coding by frame is shown, the temporal color code projection tool was used in place of the simple sum projection.

Supplementary Text

A note on the interpretation of drug treatments on ER motion

At first glance, the ability of a wide range of drugs to alter or reduce ER motion is an intriguing but puzzling finding, since the pharmacological treatments selected affect highly diverse components of cellular biology. However, despite their apparent diversity, all of the treatments used target systems within the cell that are known to be major consumers of cellular energy sources. A number of studies have suggested that living cells have local fluctuations in cytoplasmic pressure as a result of many active intracellular forces, some of which have known origins (*22*-*25*). These fluctuations are dependent on cellular energy sources. These cytoplasmic variations in local pressure seemed a possible source for ER motion. Consequently, drug treatments were selected to target several of the most fundamental, energy-consuming processes in cells, and it is thus not surprising that they had markedly similar and dramatic effects on ER motion. Some notes on the reason for selecting each treatment are given below:

Depletion of cellular ATP was achieved using DOG + NaN_3 as has been previously characterized, and the treatment was independently verified to have been functional by confirming the significant reduction of motion in the actin cytoskeleton (data not shown). This treatment has been previously demonstrated to reduce cytoplasmic fluctuations to a level consistent with purely thermal contributions after 1 h of treatment (*26*).

Block of access to cellular energy sources was accomplished by treatment with AlF, which locks trimeric G-proteins in a false GTP-bound state. This condition has been shown to broadly block cellular access to energy stored in the form of GTP and a significant proportion of energy stored in the form of ATP.

Inhibition of a major subset of actomyosin-based motor proteins was achieved by treatment with a high concentration of Blebbistatin, a myosin II inhibitor. This drug has previously been demonstrated to halt a significant proportion of actin cytoskeleton dynamics and is known to substantially reduce cytoplasmic fluctuations (*26*).

Microtubule depolymerization was attained using a high dose of nocodazole, as microtubule-based motor proteins are thought to be a substantial contributor to cytoplasmic motion (*27*).

Cellular translation was blocked using two separate treatments, one that leaves the ribosome-RNA complex intact (CHX) and another that causes its dissociation (Puromycin). Both of these reduced ER motion in a similar manner to energy depletion. Translation has been estimated to be the utilizer of up to 20% of cellular energy (reviewed in (*28*)), but to the best of our knowledge it has not been directly tested as a source of cytoplasmic motion.

We therefore conclude that ER motion appears to be broadly linked to cellular energy consumption, but it is not yet clear if this is the direct result of cellular forces causing random motion in the cytoplasm or not.

A note on the size and lifespan of spaces

As reported in the main text, the relocation of the fluorescent protein tag from the membrane (Sec61β) to lumen of the ER (ER3) results in the appearance of smaller diameter tubules and thus larger measureable gaps between tubules. Thus, a luminal marker, such as ER3, not only gives the appearance of larger distances between tubules, but also allows smaller spaces between the tubules to be measured. We find there is a direct correlation between the size and lifespan of spaces (data not shown), with larger spaces lasting longer than small spaces. It then follows that with a luminal ER marker, more short lived spaces can be measured due to the ability to distinguish between more tightly packed tubules, as seen in Fig. 2D and tables S3 and S4. These results are most consistent with a model of the ER that is a dense array of tubular matrices as opposed to fenestrated sheets. Assuming that tubes and junction on average are moving at similar speeds, the spaces between them would then disappear more quickly if the tubes are closer and more slowly if the tubes are sparse.

Rationale for the selection of FIB-SEM

The optical imaging techniques presented in this paper are able to resolve the structure of ER matrices most readily in the thin periphery of cells, where the cell is in the range of hundreds of nanometers thick. Indeed, when we measure the span between plasma membranes in a FIB-SEM cross-section, we find the distance to average 900 ± 300 nm (fig. S5). While it is possible that ER matrices are also located in the thicker, denser regions of the cell closer to the nucleus, it seemed prudent to choose an electron microscopy approach that would maximize our chances of (i) finding structures in thin regions of cells that are close to the coverslip and (ii) being able to resolve structures that may exist within this small range above the coverslip.

Most successful three dimensional EM reconstructions of the ER have been performed using serial-section or serial block-face scanning approaches (*29*, *30*). While these approaches are optimal for tissue sections, they can be technically challenging to perform on coverslip-grown cells where the region abutting the coverslip is of critical importance. By contrast, traditional approaches for this region, such as cellular unroofing followed by platinum replica EM, do not leave the ER attached to the sample, while whole-mount approaches fail to provide sufficient information in the *z* dimension. FIB-SEM has been successfully used to look in a variety of tissues and cell types, and provides an advantage in that milling using a fine atomic beam can result in *z* steps as fine as the resolution in *x* and *y*. In our experiments, this resulted in isotropic 8 nm voxels, which substantially simplified the registration process and avoided many of the issues that can complicate serial section approaches such as tears, folds, and damaged slices. In practice, this also greatly improved our ability to appreciate small height changes in thin structures like many ER matrices. For example, the raw FIB-SEM data for the region in the box shown in Fig. 5A is shown compared to simulated data that would be acquired using a serial sectioning technique with 32 nm slices (fig. S6).

Notes on protein heterogeneity in ER matrices

At first glance, the heterogeneity of ER shaping protein localization within matrices is quite curious. The localization of RTN isoforms and CLIMP63 (Figs. 6 and S2) are quite striking, with examples of both inclusion and exclusion for every protein tested. While antibody staining could potentially lead to low labeling density within sufficiently dense structures, this would not be predicted to affect genetic tags and overexpression experiments. Conversely, overexpression could drive internalization of proteins into structures where they would not otherwise be located, but this would not be seen in endogenous labeling. Thus, we conclude that at least for some ER shaping proteins (i.e. RTN4A/B + CLIMP63), there may be distinct subsets of ER matrix where the proteins can be enriched, present, or excluded. Whether this correlates with the highly variable matrix structures observed in FIB-SEM (Fig. 5) remains to be seen.

There are many variables that could contribute to this heterogeneity. It is conceivable that some RTN isoforms could be excluded from dense matrices of tubules for a variety of reasons such as: (i) enrichment of other protein within tubular matrices displacing RTNs; (ii) tubules packed at high density could have a net curvature that is incompatible with the curvature stabilizing properties of some RTN isoforms; or (ii) the highly dynamic nature of tubular matrices may be incompatible with the stability of oligomeric RTN complexes, as is evidenced by their low diffusion coefficients in a variety of studies (*31*). The role of CLIMP63 in these structures is less clear. Certainly,

CLIMP63 has been implicated in stabilizing the luminal spacing in intact sheets (at approximately 50 nm, (*2*)), but there is no *a priori* reason why it may not also be able to stabilize the luminal diameter of tubules or tubular matrices in a similar way. Furthermore, serial section EM studies in primary neurons have implicated CLIMP63 in causing regions of ER complexity, which are "not sheet-like" in nature (*32*), suggesting this protein may also be able to play an important role in producing and maintaining tubular structures.

Atlastin Isoform Usage

Exogenous expression experiments using ATLs were performed using ATL1 due to the availability of reagents and extensive literature on the protein (*33*). The cellular localization of HaloTag-ATL1 construct was verified by cotransfecting HeLa cells with mEmerald-Sec61β, HaloTag-ATL1 and Myc-ATL1 (fig. S7). Immunocytochemistry was carried out as detailed above. Both ATL1 constructs localize to the ER, demonstrating high colocalization with one another in the periphery. Any minor discrepancies in localization between the Myc- and HaloTag-ATL1 in the perinuclear region are likely due to antibody penetration during the staining protocol.

For endogenous localization experiments, we utilized an antibody to ATL3 since this is the predominant ATL isoform in most non-neuronal cell lines. ATL3 is believed to function in a homologous manner to ATL1 (*34*). Furthermore, in HeLa cells overexpressing mEmerald-Sec61β, HA-ATL3 and Myc-ATL1, both ATL isoforms localize to very similar regions of peripheral ER (fig. S8).

References:

1. P.-P. Zhu, C. Soderblom, J.-H. Tao-Cheng, J. Stadler, C. Blackstone, SPG3A protein atlastin-1 is enriched in growth cones and promotes axon elongation during neuronal development. *Human Molecular Genetics*. **15**, 1343–1353 (2006).

2. Y. Shibata *et al.*, Mechanisms determining the morphology of the peripheral ER. *Cell*. **143**, 774–788 (2010).

3. J. Riedl *et al.*, Lifeact: a versatile marker to visualize F-actin. *Nat Meth*. **5**, 605–607 (2008).

4. W. He *et al.*, Reticulon family members modulate BACE1 activity and amyloid-β peptide generation. *Nat Med*. **10**, 959–965 (2004).

5. C. W. Lai, D. E. Aronson, E. L. Snapp, BiP availability distinguishes states of homeostasis and stress in the endoplasmic reticulum of living cells. *Mol. Biol. Cell*. **21**, 1909–1921 (2010).

6. E. L. Snapp, A. Sharma, J. Lippincott-Schwartz, R. S. Hegde, Monitoring chaperone engagement of substrates in the endoplasmic reticulum of live cells. *Proc Natl Acad Sci USA*. **103**, 6536–6541 (2006).

7. J. B. Grimm *et al.*, A general method to improve fluorophores for live-cell and

single-molecule microscopy. *Nat Meth*. **12**, 244–250 (2015).

8. N. B. Cole, Compendium of drugs commonly used in cell biology research. *Current Protocols in Cell Biology*, 00:1B:1.B.1–1.B.26 (1998).

9. J. G. Donaldson, R. A. Kahn, J. Lippincott-Schwartz, R. D. Klausner, Binding of ARF and beta-COP to Golgi membranes: possible regulation by a trimeric G protein. *Science*. **254**, 1197–1199 (1991).

10. D. Li *et al.*, Extended-resolution structured illumination imaging of endocytic and cytoskeletal dynamics. *Science*. **349**, aab3500–aab3500 (2015).

11. J. A. Steyer, W. Almers, A real-time view of life within 100 nm of the plasma membrane. *Nature Reviews Molecular Cell Biology*. **2**, 268–275 (2001).

12. W. R. Legant *et al.*, High-density three-dimensional localization microscopy across large volumes. *Nat Meth*. **13**, 359–365 (2016).

13. B.-C. Chen *et al.*, Lattice light-sheet microscopy: Imaging molecules to embryos at high spatiotemporal resolution. *Science*. **346**, 1257998–1257998 (2014).

14. T. J. Deerinck, E. A. Bushong, A. Thor, M. H. Ellisman, NCMIR methods for 3D EM: A new protocol for preparation of biological specimens for serial block face scanning electron microscopy. *Microscopy*, 6–8 (2010).

15. P. Kner, B. B. Chhun, E. R. Griffis, L. Winoto, M. G. L. Gustafsson, Super-resolution video microscopy of live cells by structured illumination. *Nat Meth*. **6**, 339–342 (2009).

16. C. Sommer, C. Straehle, U. Kothe, F. A. Hamprecht, Ilastik: Interactive learning and segmentation toolkit. *2011 8th IEEE International Symposium on Biomedical Imaging (ISBI 2011)*, 230–233 (2011).

17. I. Arganda-Carreras, R. Fernández-González, A. Muñoz-Barrutia, C. Ortiz-De-Solorzano, 3D reconstruction of histological sections: Application to mammary gland tissue. *Microsc. Res. Tech.* **73**, 1019–1029 (2010).

18. K. Jaqaman *et al.*, Robust single-particle tracking in live-cell time-lapse sequences. *Nat Meth*. **5**, 695–702 (2008).

19. R. Metzler, J. Klafter, The random walk's guide to anomalous diffusion: a fractional dynamics approach. *Physics Reports*. **339**, 1–77 (2000).

20. D. Loerke *et al.*, Cargo and dynamin regulate clathrin-coated pit maturation. *PLoS Biol.* **7**, e57 (2009).

21. A. V. Weigel, M. M. Tamkun, D. Krapf, Quantifying the dynamic interactions between a clathrin-coated pit and cargo molecules. *Proc. Natl. Acad. Sci. U.S.A.*

110, E4591–600 (2013).

22. A. D. Doyle, K. M. Yamada, Cell biology: Sensing tension. *Nature*. **466**, 192–193 (2010).

23. Y. F. Dufrêne *et al.*, Five challenges to bringing single-molecule force spectroscopy into living cells. *Nature Publishing Group*. **8**, 123–127 (2011).

24. G. G. Gundersen, H. J. Worman, Nuclear Positioning. *Cell*. **152**, 1376–1389 (2013).

25. C.-P. Heisenberg, Y. Bellaïche, Forces in Tissue Morphogenesis and Patterning. *Cell*. **153**, 948–962 (2013).

26. M. Guo *et al.*, Probing the Stochastic, Motor-Driven Properties of the Cytoplasm Using Force Spectrum Microscopy. *Cell*. **158**, 822–832 (2014).

27. R. D. Vale, The Molecular Motor Toolbox for Intracellular Transport. *Cell*. **112**, 467–480 (2003).

28. D. F. Rolfe, G. C. Brown, Cellular energy utilization and molecular origin of standard metabolic rate in mammals. *Physiol. Rev.* **77**, 731–758 (1997).

29. M. Puhka, M. Joensuu, H. Vihinen, I. Belevich, E. Jokitalo, Progressive sheet-to-tubule transformation is a general mechanism for endoplasmic reticulum partitioning in dividing mammalian cells. *Mol. Biol. Cell*. **23**, 2424–2432 (2012).

30. M. Puhka, H. Vihinen, M. Joensuu, E. Jokitalo, Endoplasmic reticulum remains continuous and undergoes sheet-to-tubule transformation during cell division in mammalian cells. *J Cell Biol*. **179**, 895–909 (2007).

31. Y. Shibata *et al.*, The reticulon and DP1/Yop1p proteins form immobile oligomers in the tubular endoplasmic reticulum. *J. Biol. Chem.* **283**, 18892–18904 (2008).

32. T. Cui-Wang *et al.*, Local Zones of Endoplasmic Reticulum Complexity Confine Cargo in Neuronal Dendrites. *Cell*. **148**, 309–321 (2012).

33. U. Goyal, C. Blackstone, Untangling the web: Mechanisms underlying ER network formation. *BBA - Molecular Cell Research*. **1833**, 2492–2498 (2013).

34. N. Rismanchi, C. Soderblom, J. Stadler, P.-P. Zhu, C. Blackstone, Atlastin GTPases are required for Golgi apparatus and ER morphogenesis. *Human Molecular Genetics*. **17**, 1591–1604 (2008).

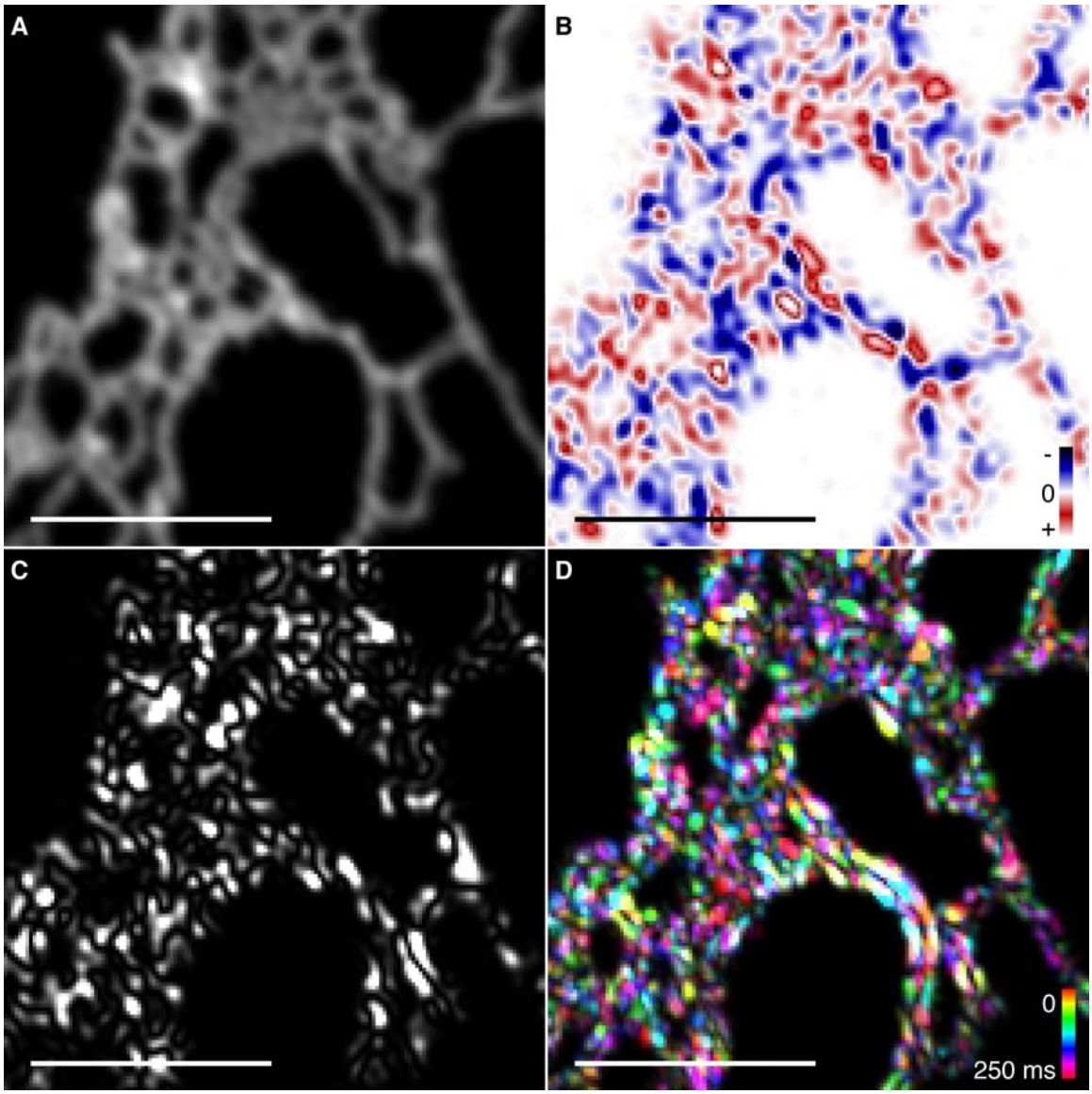

Fig. S1.

Method for temporal derivative. **(A)** An image acquired and reconstructed by GI-SIM, smoothed using a Gaussian filter with σ = 45 nm and bleach corrected using the histogram-matching algorithm in ImageJ. **(B)** Each frame is subtracted from the subsequent frame. **(C)** The resulting image is squared. **(D)** The derivative is temporally color-coded over the length of the time-lapse image. Scale bars, 2 μm.

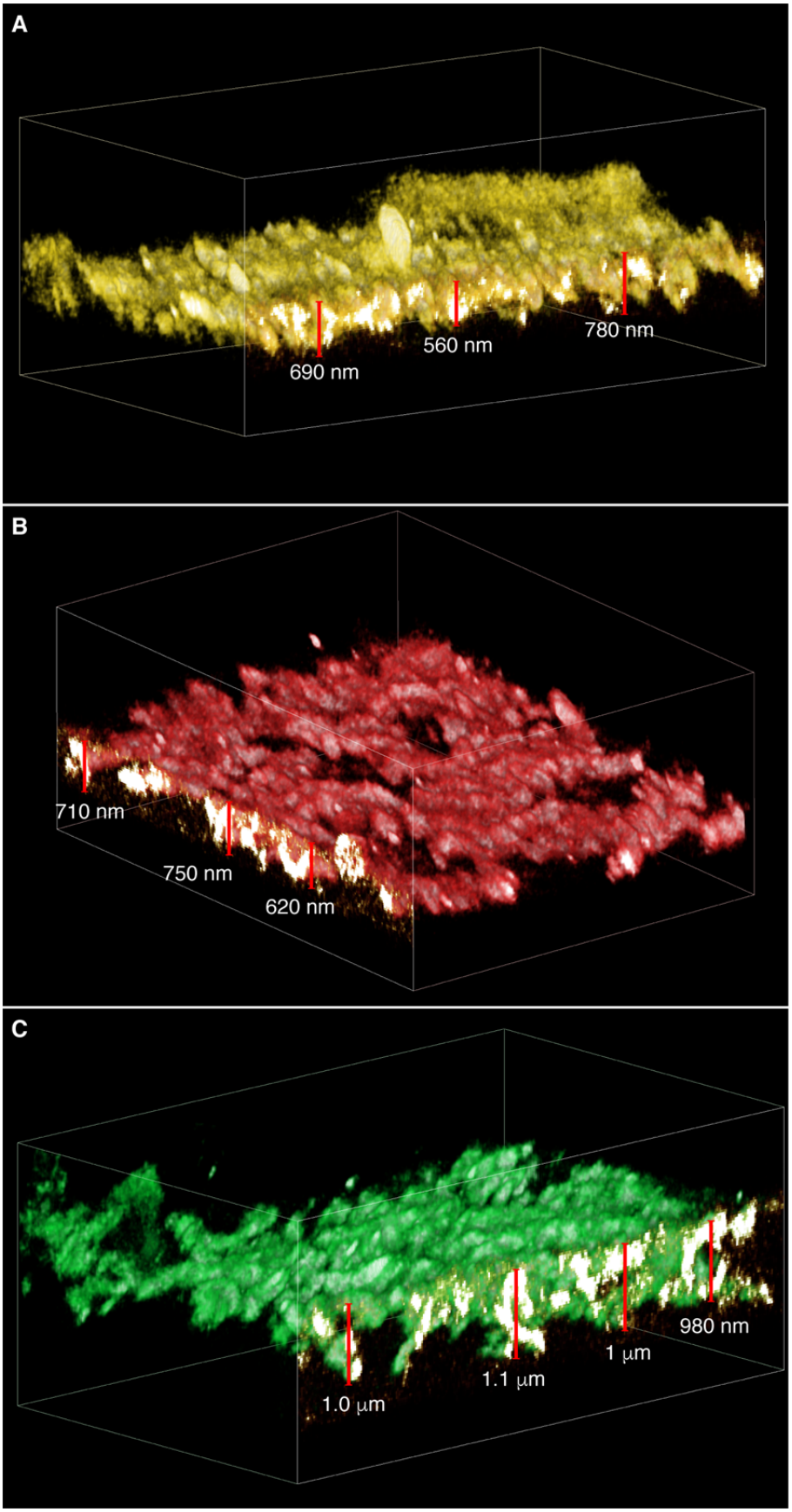
A
690 nm
560 nm
780 nm
B
710 nm
750 nm
620 nm
C
1.0 μm
1.1 μm
1 μm
980 nm

Fig. S2.

The ER is three-dimensional in nature even in thin regions of the cell. (A-C) Cross-sections through the LLS-PAINT data shown in Fig. 3B. Despite some ER matrices being relatively flat, when imaged with sufficiently high resolution in the *z* dimension substantial topology can be observed.

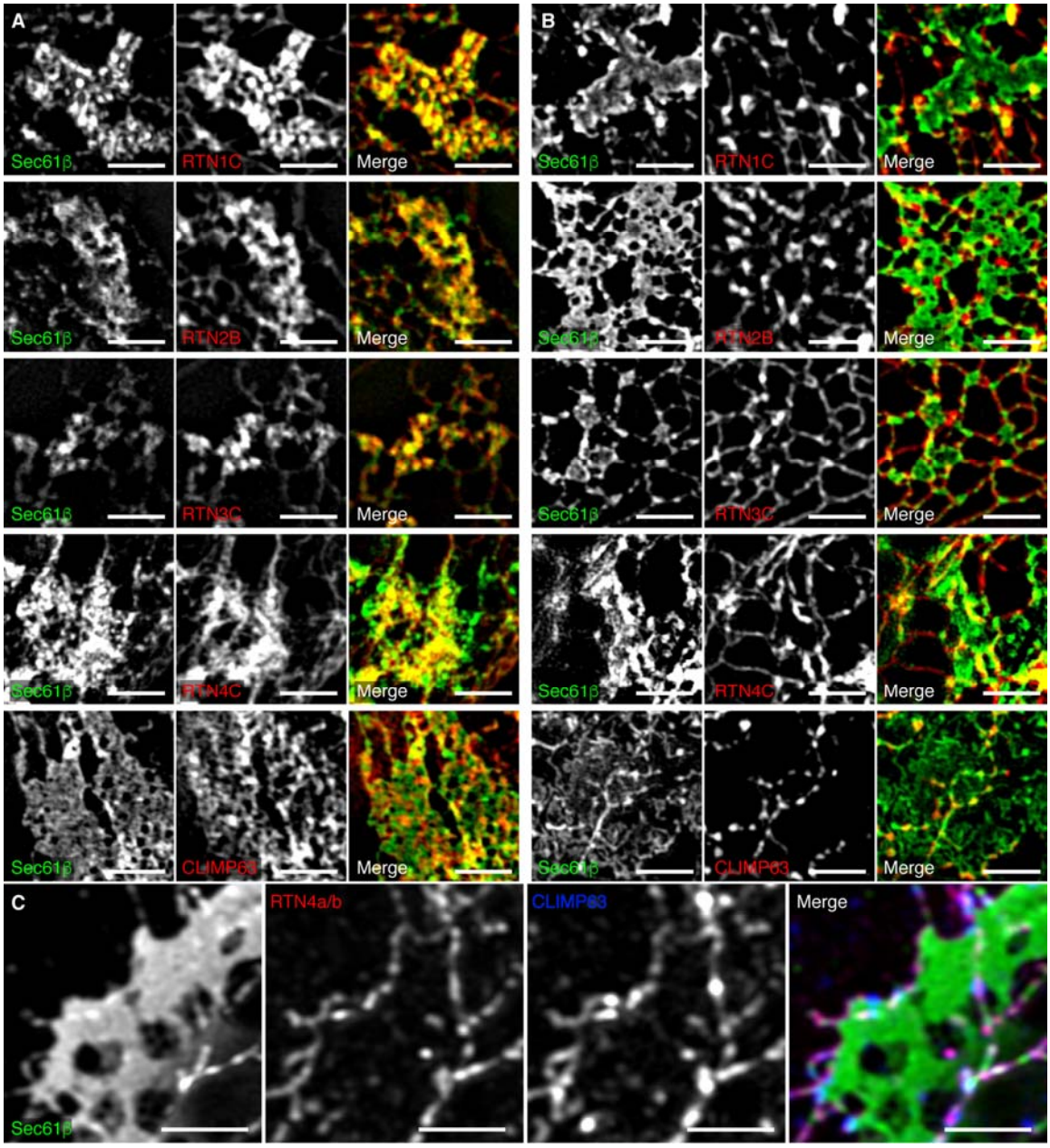

Fig. S3.

Traditional ER-shaping proteins show heterogeneity in matrix localization. Fixed COS-7 cells expressing mEmerald-Sec61β and an ER-shaping protein imaged by 3D-SIM. Examples of inclusion **(A)** within dense tubular matrices and exclusion **(B)** for each ER shaping protein. **(C)** A U-2 OS cell expressing mEmerald-Sec61β stained for endogenous RTN4A/B and CLIMP63, illustrating exclusion from a dense tubular matrix. Scale bars, 2 μm.

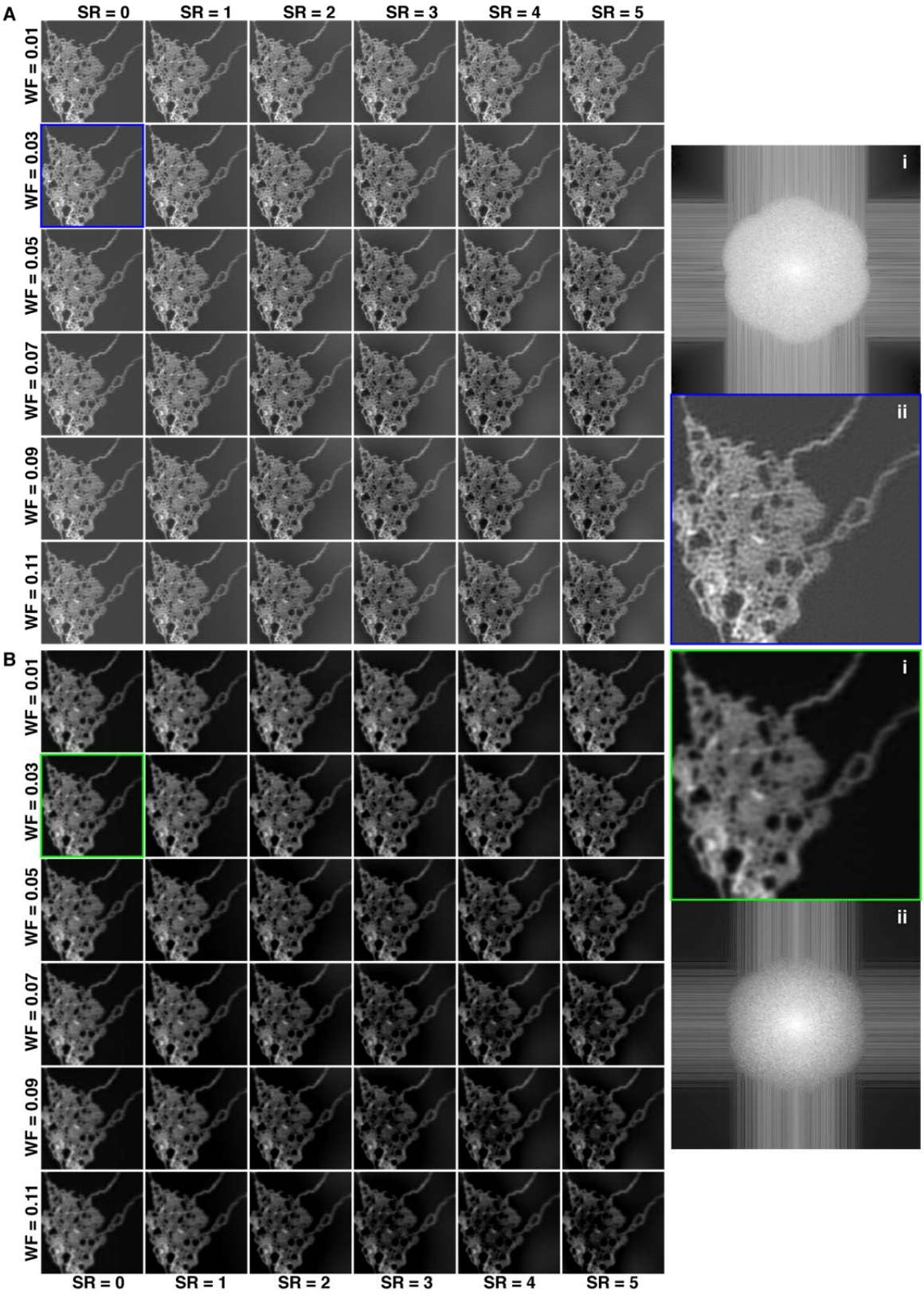
A
SR = 0
SR = 1
SR = 2
SR = 3
SR = 4
SR = 5
WF = 0.01
WF = 0.03
WF = 0.05
WF = 0.07
WF = 0.09
WF = 0.11
i
ii
B
WF = 0.01
WF = 0.03
WF = 0.05
WF = 0.07
WF = 0.09
WF = 0.11
SR = 0
SR = 1
SR = 2
SR = 3
SR = 4
SR = 5
i
ii

Fig. S4.

Optimization of SIM reconstructions. A comprehensive analysis of critical SIM reconstruction steps to minimize any reconstruction-based artifacts. **(A)** Wiener filter vs a notch filter localized at the peaks at Abbe's limit, with the indicated suppression radius (SR), no Gaussian blurring. **(B)** Wiener filter vs a notch filter (as above), with $\sigma = 45$nm radius Gaussian blur. Colored boxes **(i)** denote settings that were used for this particular image (WF = 0.03, SR = 0) with (green box) and without (blue box) Gaussian blurring and their corresponding optical transfer function **(ii)**.

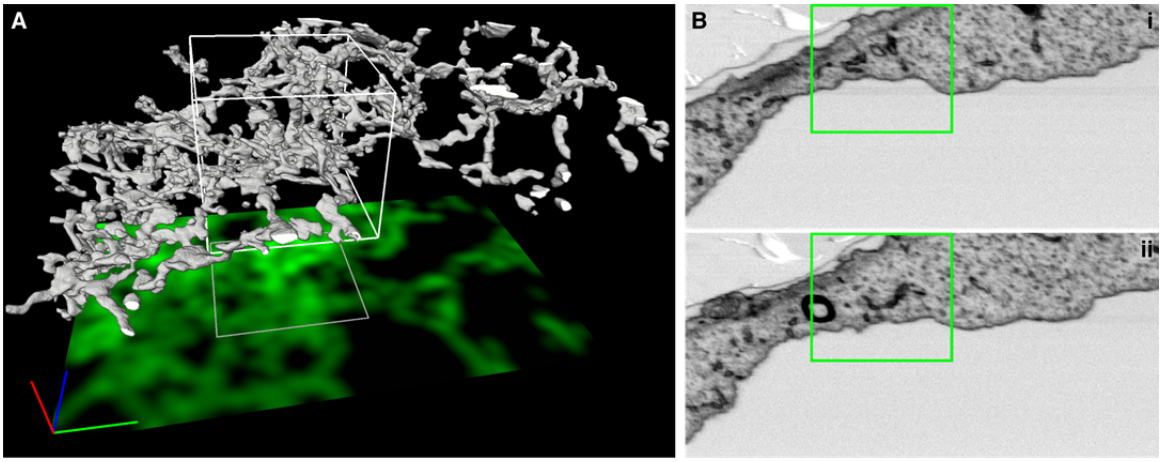

Fig. S5.

Measuring the thin periphery of cells. (A) FIB-SEM reconstruction of an ER matrix, reproduced from Fig. 5B. **(B)** FIB-SEM slices of the area in (A) in the *x*-*z* plane (red-green axis) with boxed region shown for orientation. Slices **(i)** and **(ii)** are spaced by 800 nm in *y* (blue axis). The distance between the plasma membranes within the boxed region is 900 ± 300 nm (n = 21 measurements).

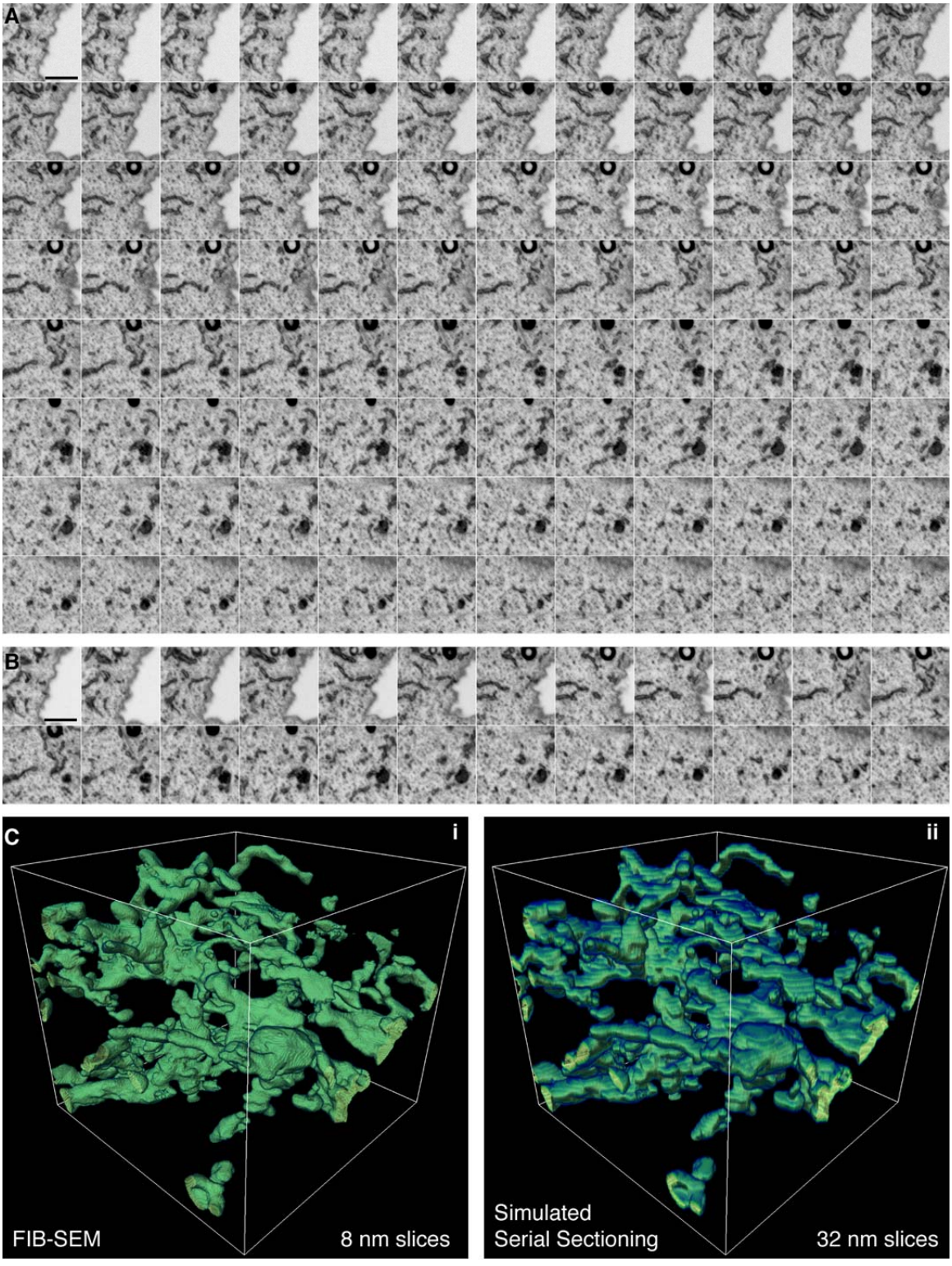

Fig. S6

FIB-SEM provides more information about small changes in z-height than traditional serial section techniques. The raw data collected in the volume indicated by the box in Figure 5B (2.4 x 2.4 μm). **(A)** FIB-SEM using 8 nm steps collects 96

individual slices through this region (786 nm). Scale bar, 1 μm. **(B)** Simulated data collected using a serial section technique with 32 nm thickness per slice (sum of 4 serial FIB-SEM slices) through the same region. Scale bar, 1 μm. **(C)** 3D reconstruction of slices in **(i)** (A) and **(ii)** (B). The loss of detail can be seen in the theoretical serial section technique.

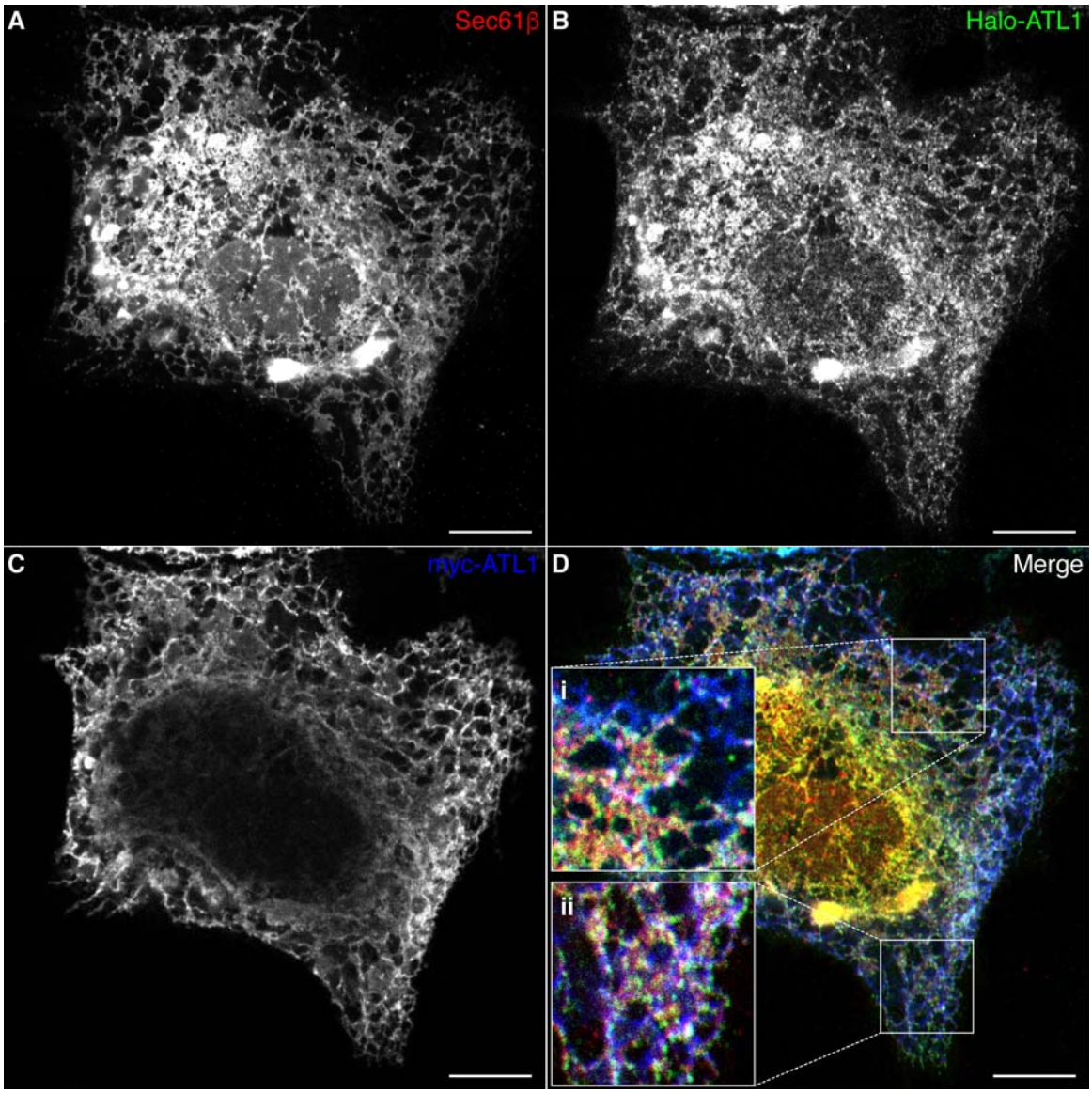

Fig. S7

Introduction of a HaloTag does not perturb ATL1 localization to tubular ER structures. **(A-C)** Fixed HeLa cell expressing mEmerald-Sec61β **(A)**, HaloTag-ATL1 **(B)**, and Myc-ATL1 **(C)** were imaged by scanning point confocal microscopy. **(D)** HaloTag-ATL1 and Myc-ATL1 colocalize at similar regions of ER. The two insets, **(i)** and **(ii)**, in the merged image demonstrate localization of both Myc-ATL1 and HaloTag-ATL1 within structures that appear as sheets. Scale bars, 10 μm.

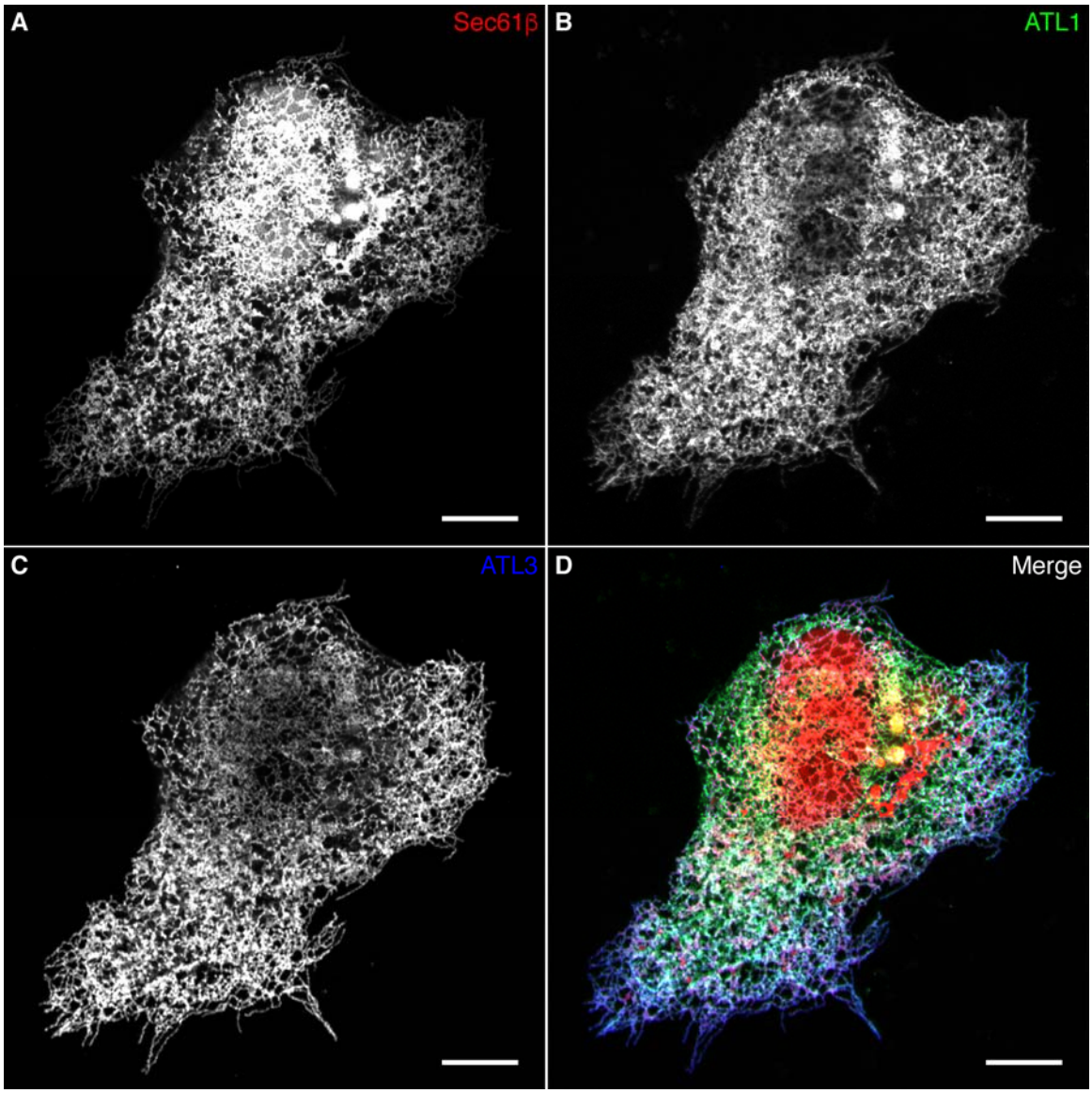

Fig. S8

ATL1 and ATL3 co-localization. Fixed HeLa cell co-expressing mEmerald-Sec61β. (A), Myc-ATL1 **(B)**, and HA-ATL3 **(C)** was imaged using scanning point confocal microscopy. The merged image **(D)** shows that Myc-ATL1 and HA-ATL3 co-localize within similar regions of the ER. Scale bars, 10 μm.

Table S1.

Summary of measurements reported in Fig. 1. The mean peak-to-peak amplitude (Figs. 1C, 1E) and frequency of oscillations (Fig. 1D, 1E) is stated for each treatment, as well as the measured MSD alpha exponents (Fig. 1G) of three-way junctions.

	Condition	*N* (tubules)	*N* (cells)	Amplitude ± SD (nm)	Frequency ± SD (Hz)
Figure 1C, 1D & 1E	Sec61β	1755	8	70 ± 50	4 ± 1
	ER3	3230	19	70 ± 50	4 ± 1
	U-2 OS - Sec61β	610	9	60 ± 50	4 ± 1
	DOG + NaN_3	1080	9	40 ± 20	8 ± 2
	AlF	1291	8	40 ± 20	9 ± 2
	NZ	413	5	70 ± 30	7 ± 2
	Bleb	698	4	40 ± 20	9 ± 3
	Puro	1105	5	40 ± 20	9 ± 2
	CHX	1017	5	50 ± 20	9 ± 2

	Condition	*N* (junctions)	*N* (cells)	Alpha ± SD
Figure 1G	Sec61β	313	8	0.5 ± 0.3
	ER3	279	19	0.4 ± 0.2
	U-2 OS - Sec61β	148	9	0.4 ± 0.2
	DOG + NaN_3	273	9	0.1 ± 0.2
	AlF	186	8	0.2 ± 0.2
	NZ	57	5	0.3 ± 0.3
	Bleb	135	4	0.1 ± 0.2
	Puro	211	5	0.2 ± 0.2
	CHX	134	5	0.2 ± 0.2

Table S2.

Testing the populations in Fig. 1 for statistically significant differences in means. A one-way ANOVA was used to test for significant differences between means of the three groups: Sec61bβ, ER3 and U-2 OS - Sec61β. Tukey's multiple comparison post hoc test was then used to test between specific groups. A two-tailed, two sample *t*-test using a Welch correction for non-equal variance was used to test between control (Sec61bβ) and drug treatment groups. Highlighted cells denote statistical significance at the 0.001 level.

ONE-WAY ANOVA

Group 1	*Group 2*	*Group 3*	*Mean amplitude p-value*	*Mean frequency p-value*	*Mean alpha p-value*
Sec61β	ER3	U-2 OS - Sec61β	0.024	2.7E-4	2.2E-4

TUKEY'S MULTIPLE COMPARISON POST HOC TEST

	Group 1	*Group 2*	*Mean amplitude p-value*	*Mean frequency p-value*	*Mean alpha p-value*
	Sec61β	ER3	0.99	0.0089	0.013
	Sec61β	U-2 OS - Sec61β	0.031	0.38	3.6E-4
	ER3	U-2 OS - Sec61β	0.024	0.0020	0.30

TWO SAMPLE *T*-TEST WITH WELCH CORRECTION FOR NON-EQUAL VARIANCE

	Group 1	*Group 2*	*Mean amplitude p-value*	*Mean frequency p-value*	*Mean alpha p-value*
	Sec61β	DOG + NaN_3	1.9E-82	< 1E-230	1.1E-64
	Sec61β	AlF	2.2E-138	< 1E-230	1.2E-47
	Sec61β	NZ	0.54	3.56E-103	1.1E-6
	Sec61β	Bleb	3.6E-137	4.82E-229	1.4E-42
	Sec61β	Puro	1.9E-100	< 1E-230	6.4E-34
	Sec61β	CHX	5.6E-62	< 1E-230	3.3E-30

Table S3.

Summary of measurements reported in Fig. 2. Lifetime of spaces extracted from SPT of inverted sheets (Fig. 2D, top), distance between dense tubules (Fig. 2D, bottom)

	Condition	*N* (spaces)	*N* (cells)	Lifetime ± SD (ms)
Figure 2D (top)	Sec61β	4292	4	250 ± 250
	ER3	1986	5	190 ± 160
	U-2 OS - Sec61β	2009	4	260 ± 240
	Condition	***N* (spaces)**	***N* (cells)**	**Distance ± SD (nm)**
Figure 2D (bottom)	Sec61β	1273	4	260 ± 350
	ER3	1913	5	310 ± 370
	U-2 OS - Sec61β	650	4	300 ± 490

Table S4.

Testing the populations in Figure 2 for statistically significant differences in means. A one-way ANOVA was used to for significant differences between means of the three groups: Sec61bβ, ER3 and U-2 OS - Sec61β. Tukey's multiple comparison post hoc test was then used to test between specific groups. Highlighted cells denote statistical significance at the 0.001 level.

ONE WAY ANOVA

Group 1	*Group 2*	*Group 3*	*Mean lifetime p-value*	*Mean distance p-value*
Sec61β	ER3	U-2 OS - Sec61β	< 1E-230	0.0056

TUKEY'S MULTIPLE COMPARISON POST HOC TEST

	Group 1	*Group 2*	*Mean lifetime p-value*	*Mean distance p-value*
	Sec61β	ER3	3.3E-16	0.0044
	Sec61β	U-2 OS - Sec61β	0.70	0.12
	ER3	U-2 OS - Sec61β	3.3E-16	0.90

Table S5.

Summary of measurements reported in Fig. 4. The effect of temporal blurring (Fig. 4B) and spatial resolution (Fig 4C) on the diameter of tubules. The effect of temporal blurring on the measurable distance between dense tubules (Fig. 4E) and density of spaces (Fig 4F). The effect of spatial blurring on the measurable distance between dense tubules (Fig. 4H) and density of spaces (Fig. 4I).

Figure 4B (live)	**Condition**	***N* (tubes)**	***N* (cells)**	**Diameter ± SD (nm)**
	25 ms	90	3	200 ± 30
	250 ms	92	5	200 ± 20
	1 s	91	5	220 ± 30
Figure 4C (fixed)	**Condition**	***N* (tubes)**	***N* (cells)**	**Diameter ± SD (nm)**
	GI	59	2	270 ± 30
	3D-SIM	145	3	150 ± 20
	PAINT	152	3	120 ± 40
Figure 4E (live)	**Condition**	***N* (spaces)**	***N* (cells)**	**Distance ± SD (nm)**
	25 ms	74	3	150 ± 50
	250 ms	144	5	310 ± 30
	1 s	145	5	410 ± 50
Figure 4F (live)	**Condition**	***N* ("sheets")**	***N* (cells)**	**Density ± SD (μm^{-2})**
	25 ms	18	3	7 ± 3
	250 ms	18	5	5 ± 3
	1 s	18	5	4 ± 2
Figure 4H (fixed)	**Condition**	***N* (spaces)**	***N* (cells)**	**Distance ± SD (nm)**
	GI	131	2	500 ± 200
	3D-SIM	162	4	220 ± 80
	PAINT	46	3	200 ± 200
Figure 4I (fixed)	**Condition**	***N* ("sheets")**	***N* (cells)**	**Density ± SD (μm^{-2})**
	GI	9	2	0.7 ± 0.2
	3D-SIM	30	4	5 ± 1
	PAINT	24	3	7 ± 3

Table S6.

Testing the populations in Figure 4 for statistically significant differences in means. A one-way ANOVA was used to for significant differences between means of the three groups in live (25 ms, 250 ms, 1 s) and fixed (GI, 3D-SIM, PAINT) cells. Tukey's multiple comparison post hoc test was then used to test between specific groups. Highlighted cells denote statistical significance at the 0.001 level.

ONE WAY ANOVA

Group 1	*Group 2*	*Group 3*	*Mean tube diameter p-value*	*Mean distance across spaces p-value*	*Mean density of spaces p-value*
25 ms	250 ms	1 s	2.5E-5	2.1E-6	3.2E-4
GI	3D-SIM	PAINT	< 1E-230	< 1E-230	6.3E-10

TUKEY'S MULTIPLE COMPARISON TEST

	Group 1	*Group 2*	*Mean tube diameter p-value*	*Mean distance across spaces p-value*	*Mean density of spaces p-value*
Live	25 ms	250 ms	0.12	0.0052	0.053
	25 ms	1 s	1.4E-5	1.0E-6	1.97E-4
	250 ms	1 s	0.019	0.035	0.13
Fixed	GI	3D-SIM	< 1E-230	< 1E-230	2.16E-7
	GI	PAINT	< 1E-230	< 1E-230	< 1E-230
	3D-SIM	PAINT	< 1E-230	0.44	0.024

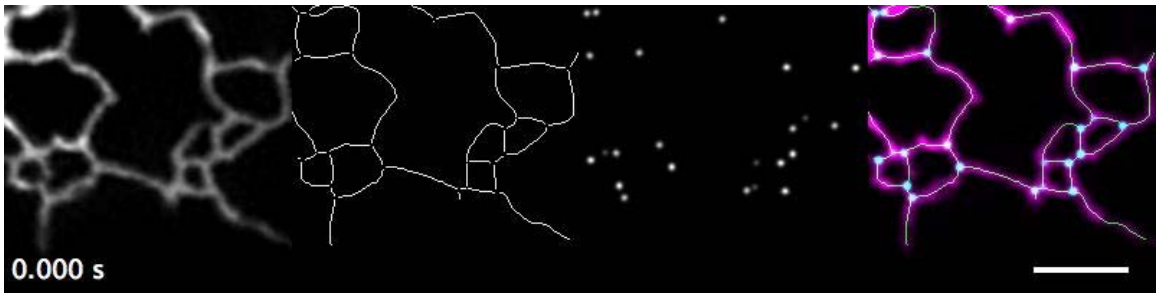

Movie S1.

Tracking of rapid motions of peripheral ER tubules and three-way junctions. A region of a COS-7 cell overexpressing mEmerald-Sec61β imaged at 40 Hz using GI-SIM (leftmost panel). The skeletonized midline of each tubule is depicted in the middle-left panel from which its motion can be calculated (e.g., Fig. 1C). The location of three-way junctions is depicted in the middle-right panel, from which a SPT algorithm was used to extract dynamics (e.g., Fig. 1E). Overlay of all three panels is shown at right. Scale bar, 2 μm.

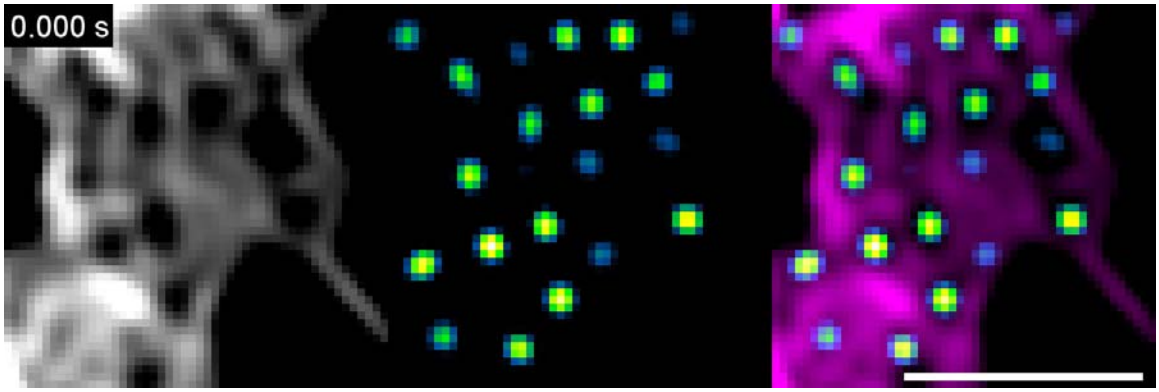

Movie S2.

Peripheral ER "sheets" appear discontinuous. A peripheral sheet from a COS-7 cell overexpressing mEmerald-Sec61β imaged at 40 Hz using GI-SIM (left panel). The middle panel illustrates spaces within the "sheet" derived from inverting the image, subtracting the area outside of the "sheet", and Gaussian smoothing (see Materials and Methods). This permits SPT of spaces. A merge of both the raw data and data processed for illustrating spaces is depicted in the right panel. Scale bar, 2 μm.

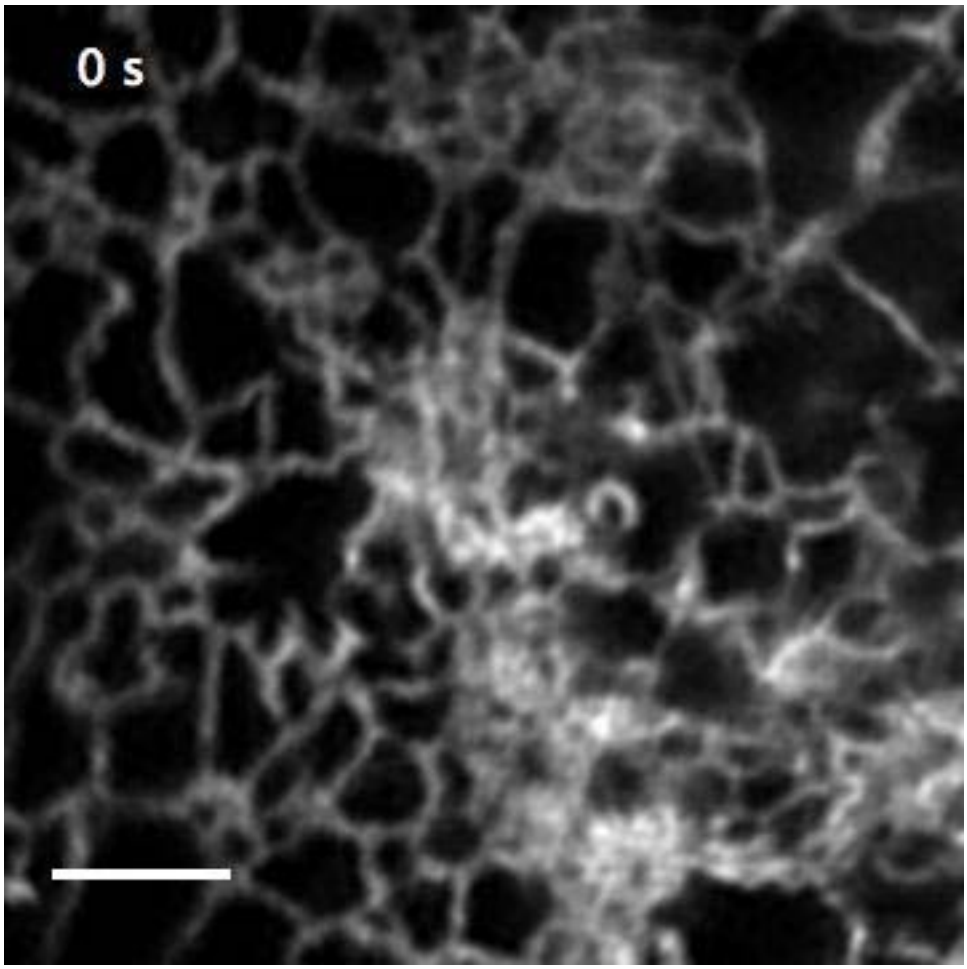

Movie S3.

Rapid assembly and disassembly of peripheral sheet-like structures into tubules. Representative region of a COS-7 cell overexpressing mEmerald-Sec61β imaged using GI-SIM. Each frame was acquired in 25 ms, with a 1 s interval between frames. Rapid moving clusters of tubules and associated three-way junctions appear to rapidly interconvert between 'sheet-like' and clustered three-way junctions. Scale bar, 2 μm.

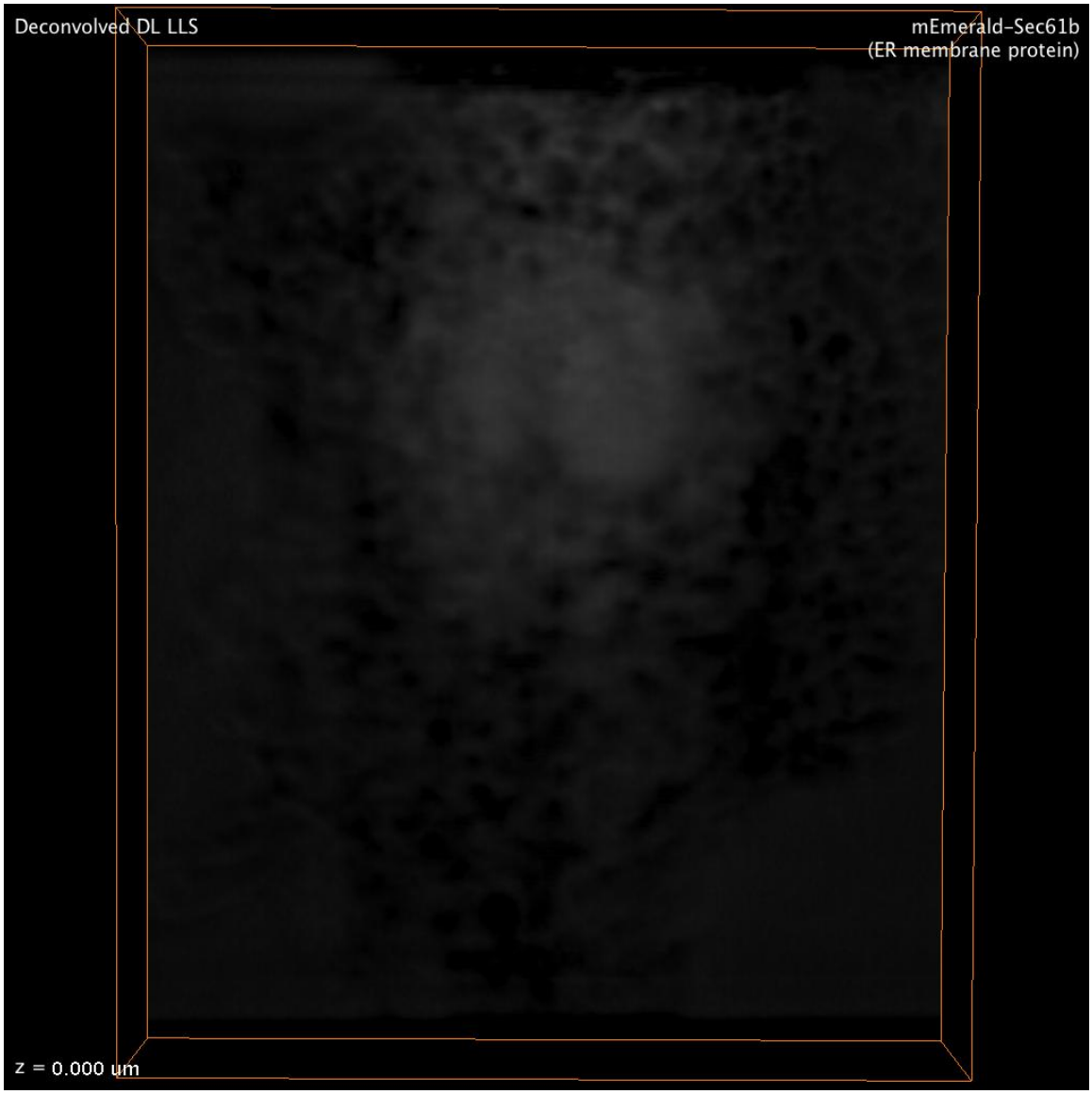

Movie S4.

Internal membranes of a fixed COS-7 cell reconstructed using correlative 3D LLS and LLS-PAINT microscopy. Correlative imaging between mEmerald-Sec61β labeled ER (gray diffraction-limited LLS image) imaged using 3D LSS microscopy, and all lipid membranes labeled with BODIPY-TR and AZEP-Rh (pseudo colored LLS-PAINT image), the latter reconstructed from 549 million localizations.

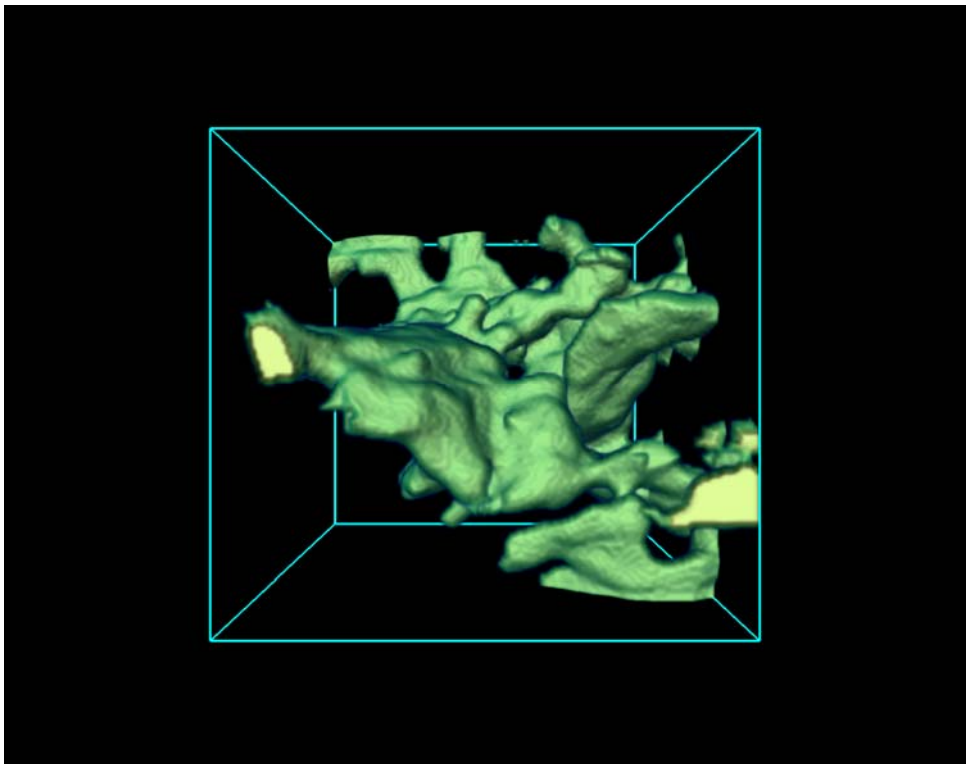

Movie S5.

The structure of a helicoidal sheet by FIB-SEM. The FIB-SEM reconstruction shown in Fig. 5F is reproduced here, to allow more clear demonstration of the helicoidal structure.